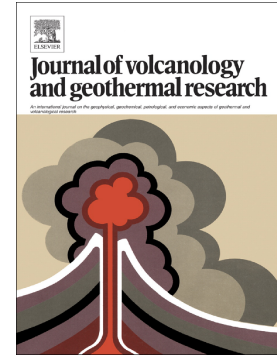# Journal Pre-proof

The role of oxides in the shallow vesiculation of ascending magmas

Alain Burgisser, Laurent Arbaret, Caroline Martel, Mélanie Forien, Mathieu Colombier

Please cite this article as: A. Burgisser, L. Arbaret, C. Martel, et al., The role of oxides in the shallow vesiculation of ascending magmas, *Journal of Volcanology and Geothermal Research* (2018), https://doi.org/10.1016/j.jvolgeores.2020.107072

This is a PDF file of an article that has undergone enhancements after acceptance, such as the addition of a cover page and metadata, and formatting for readability, but it is not yet the definitive version of record. This version will undergo additional copyediting, typesetting and review before it is published in its final form, but we are providing this version to give early visibility of the article. Please note that, during the production process, errors may be discovered which could affect the content, and all legal disclaimers that apply to the journal pertain.

The role of oxides in the shallow vesiculation of ascending magmas

Alain BURGISSER[1*], Laurent ARBARET[2], Caroline MARTEL[2], Mélanie FORIEN[3], Mathieu COLOMBIER[4]

[1] Univ. Grenoble Alpes, Univ. Savoie Mont Blanc, CNRS, IRD, IFSTTAR, ISTerre, 38000 Grenoble, France.

[2] Institut des Sciences de la Terre d'Orléans (ISTO), Université d'Orléans, CNRS, BRGM, Orléans, France.

[3] Department of Geosciences, UiT The Arctic University of Norway in Tromsø, Postboks 6050 Langnes, 9037 Tromsø, Norway.

[4] Department of Earth and Environmental Sciences, Ludwig-Maximilians-Universität München, Germany.

Abstract: 490 words, Main text: 10800 words, 12 Figures, 80 references.

* Corresponding author: Phone: (+33) 479 758 789 Email: alain.burgisser@univ-savoie.fr

Abstract

Despite their generally low volume fraction, Fe-Ti oxides have the potential to greatly influence the eruptive style because they lower the supersaturation pressure for heterogeneous bubble nucleation. Once nucleated, bubbles respond fast to pressure changes, fostering rapid expansion and explosive behavior. Yet, oxide microlite quantifications are often absent from data of explosive products. We used new, re-analyzed, and published data to build a compilation of oxide number densities (ONDs) and vesicle number densities (VNDs) of trachytic and calc-alkaline products. Four eruptive styles were selected: 1) Vulcanian explosions from Soufrière Hills volcano, Montserrat, Lascar volcano, Chile, and Kilian volcano, France, 2) blasts from Mt Pelée volcano, Lesser Antilles, Mount St. Helens, USA, and Merapi volcano, Indonesia, 3) a sub-Plinian explosion from Merapi volcano, and 4) lava dome effusions with intermittent collapse from Soufrière Hills and Mt Pelée volcanoes. Natural samples were separated into two groups according to the dominant texture of the products of each event: 1) vesicular pumice clasts from explosions with a strong vertical component

and 2) dense clasts with diktytaxitic textures from dome collapse event and lateral blast. Group 1 samples are either distributed alongside the 1:1 trend between VND and OND that spans from 10^{15} to 10^{17} m^{-3}, or have a constant VND of $10^{16–16.5}$ m^{-3} regardless of OND. A large proportion of oxides (55–100%) touch vesicles. A more variable proportion of vesicles (16–72%) are in contact with oxides because of syn-explosive growth and coalescence. Group 2 samples have ONDs in the same broad range as group 1 samples. We also used new and published data to build a compilation of ONDs and VNDs of five series of experimental decompression of rhyolitic and phonolitic melts. In samples with OND≈VND, most bubbles are in contact with more than one oxide and 64–88% of the oxides are in contact with bubbles. Such high levels of connectivity suggest that the role of oxides in controlling bubble nucleation has been underestimated. When VND≥OND, nucleation densities of experimental vesicles can be reproduced by heterogeneous nucleation models, which we used to calculate syn-explosive decompression rates from VNDs at Merapi, Soufrière Hills, and Kilian. These rates and textural evidence suggest that the decompression from accompanying these Vulcanian and sub-Plinian explosions is responsible for syn-explosive bubble nucleation. We calculated the average pre-explosive ascent rates necessary to yield the observed ONDs at Soufrière Hills and Merapi volcanoes. The resulting rates, 0.005–20 m/s, overlap considerably with the range of critical ascent rate inferred for the effusive–explosive transition, supporting the hypothesis that this transition is primarily controlled by oxide microlites in the conduit because oxides are a primer for explosive behavior when present in sufficiently high number densities. Focusing on the older eruption of Kilian, for which no observation is available, we infer that pre-explosive ascent rates of $>7\times10^{-3}$ m/s were necessary for explosive behavior to occur.

Keywords: Fe-Ti oxides; number density; bubbles; microlite; dome eruption; Vulcanian explosion

2

1 Introduction

When magma moves upwards into the crust to feed a volcanic eruption, the accompanying change in pressure causes degassing. The process of degassing starts with bubble nucleation, the kinetics of which is controlled by the presence or absence of crystals in the melt. Homogeneous nucleation occurs in pure melts and often requires large pressure changes to induce sufficient volatile supersaturation. Conversely, heterogeneous nucleation of gas bubbles on preexisting crystals can occur following significantly smaller pressure drops. Heterogeneous nucleation has recently been proposed to be the dominant mechanism occurring in nature (Shea, 2017). As a result, attention has been turned towards studying minerals that are able to lower supersaturation pressure to the smallest possible values. Minerals belonging to the solid solution of Fe-Ti oxides are ideal nucleation sites in this respect. The least effective Fe-Ti oxide is hematite, which reduces supersaturation pressures in rhyolite at 800 °C from ~200 MPa (homogeneous nucleation) to 130 MPa (Cluzel et al., 2008). The most effective mineral is magnetite because it reduces supersaturation pressure to less than 20 MPa (Gardner and Denis, 2004; Gardner, 2007; Shea et al., 2010) or even less than 5 MPa (Hurwitz and Navon, 1994), depending on melt composition and temperature. Magnetite crystals play an important role in magmatic systems because their large wetting angles cause bubbles to attach to them (e.g., Gardner and Denis, 2004). The ascent of such bubble-magnetite pairs could explain the formation of iron oxide–apatite deposits by buoyant segregation (Knipping et al., 2015) and could increase the efficiency of magma mixing by buoyancy-driven stirring (Edmonds et al., 2015).

Magnetite crystals have the potential to greatly influence the style of eruptions involving lavas that are more viscous than those found in to mafic systems. For example, in the case of a melt at water saturation, a magma-filled conduit subject to partial dome collapse is subject to a pressure variation in the order of 5–20 MPa (e.g., Taisne and Jaupart, 2008). This pressure range is similar to the supersaturation pressures causing heterogeneous nucleation on magnetite. Following Cluzel et al.

(2008) and Cáceres et al. (2020), it is thus reasonable to posit that a magma feeding a dome eruption and bearing large amounts of magnetite microlites would be more prone to nucleate gas bubbles in response to small pressure changes during an eruption than a magma bereft of magnetite. Once nucleated in the conduit, bubbles respond fast to pressure changes (e.g., Lensky et al., 2004; Giachetti et al., 2010) and the ensuing volume changes favor rapid expansion, fragmentation, and explosive behavior. Yet, the hypothesis that magnetite fosters explosive eruptions cannot be tested because of the lack of natural data published in the literature.

Amounts of magnetite in natural samples has typically been documented by reporting volume or modal fractions, which are generally small (<5 vol% on a bubble-free basis). Bubble nucleation, however, is sensitive to the number density of nucleation sites rather than to bulk volume or mass fraction of a given mineral. There are, to our knowledge, natural data on oxide number densities (OND) at explosive volcanoes for only one sample from the 1980 blast at Mount St. Helens, USA (Cashman, 1988), a few samples of Vulcanian explosions at Soufrière Hills, Montserrat (Giachetti et al., 2010; Burgisser et al., 2019), Shinmoedake, Japan (Mujin and Nakamura, 2014), and at Kilian volcano, France (Colombier et al., 2017). Extending the scope from explosive eruptions to the reservoir-related sample from the Bishop Tuff (Gualda and Anderson, 2007) and to the fully degassed Tokachi–Ishizawa obsidian lava (Sano et al., 2015) does not vastly extend the amount of available data. This contrasts strongly with the hundreds of samples that have given rise to the numerous published number densities of plagioclase and/or pyroxene microlite (e.g., Suzuki and Fujii, 2010; Martel, 2012; Muir et al., 2012).

There are more OND data for decompression experiments of water-saturated magmas (e.g., Martel and Schmidt, 2003; Shea et al., 2010), some of them specifically addressing heterogeneous bubble nucleation in the presence of oxides (Hurwitz and Navon, 1994; Gardner and Denis, 2004; Gardner, 2007; Cluzel et al., 2008; Cáceres et al., 2020). That oxide volume fraction is small has been used as a common argument to minimize its role in experimental work addressing bubble growth

(Burgisser and Gardner, 2004; Cichy et al., 2011; Fiege and Cichy, 2015).

The paucity of natural data hinders the assessment of the role of oxides in the shallow vesiculation of ascending magma. Here, we significantly extend existing data by documenting the OND and vesicle number density (VND) of 105 samples from explosive and effusive products at five volcanoes. Four eruptive styles were selected to evaluate the conjecture that the transition from effusive to explosive eruptions is primarily controlled by the presence or absence of oxide microlites in the conduit. The first style is Vulcanian explosions from Soufrière Hills volcano, Lascar volcano, Chile, and Kilian volcano. The second style is laterally directed blast from Mt Pelée volcano, Lesser Antilles, Mount St. Helens, and Merapi volcano, Indonesia. The third style is sub-Plinian convective fountain collapse from Merapi volcano. The last style is lava dome effusion with intermittent collapse from Soufrière Hills and Mt Pelée volcanoes. Events from Soufrière Hills, Kilian, and Merapi volcanoes have been included in this study also because the pre-explosive conditions of these sample series (i.e. the pressure and the porosity of each sample in the conduit prior to explosion) have been determined by prior studies (Burgisser et al., 2010; Drignon et al., 2016; Colombier et al., 2017; Burgisser et al., 2019; Colombier et al., submitted).

Natural samples give a spatial link between oxides and bubbles. Their possible genetic link is often obscured by the many transformations affecting the magma during ascent, evacuation, and final deposition at the surface. We selected new and published experimental data to aid natural data interpretation and to determine the conditions under which oxides can foster heterogeneous bubble nucleation. We chose published decompression experiments with more oxides than nucleated bubbles (Cluzel et al., 2008; Shea et al., 2010) and with more bubbles than oxides (Gardner, 2007; Gardner and Denis, 2004). We present new analysis of three representative samples of experimentally decompressed rhyolite melts (Burgisser and Gardner, 2004) because they have bubbles and oxides in equivalent numbers. Finally, we explore implications of these findings at three volcanoes by showing how oxide nucleation conditions, and thus explosivity, are linked to ascent rate and phase equilibria

relationships.

2 Methods

2.1 Sample selection

We used new data, re-analyzed data, and published data to build a compilation of ONDs and VNDs of nine sample series from four volcanoes, totaling 105 individual samples. There are eight new data series. Three series are from Soufrière Hills volcano. One of them is composed of a selection of the products of Vulcanian explosions in August–October 1997 studied by Burgisser et al. (2010). The two others are from products of block-and-ash flows generated by dome collapse on June 25, 1997 (Loughlin et al., 2002) and May 20, 2006 (Loughlin et al., 2010), respectively. One sample series was produced by the 1993 Vulcanian eruption at Lascar volcano (Mattews et al., 1997; Sparks et al., 1997). Two sample series were erupted by Mt. Pelée: one during the 1929 block-and-ash flows and the other during the 1902 blast (Martel et al., 2000). The last two analyzed series are products from the opening and paroxysmal stages of the 2010 eruption of Merapi volcano, which occurred on October 26 and November 5, respectively (Komorowski et al., 2013; Drignon et al., 2016). There is one re-analyzed series from the 9.4 ka Vulcanian eruption of Kilian volcano (Colombier et al., 2017; Colombier et al., submitted). New and re-analyzed samples are listed in Table S1 in the Supplementary Information. Published data include products emitted by Vulcanian events on February 11, 2010 (23 samples, Burgisser et al., 2019) and during August–October 1997 (8 samples, Giachetti et al., 2010) at Soufrière Hills, and during the 1980 blast at Mount St. Helens (Cashman, 1988).

We used new and published data to build a compilation of ONDs and VNDs of five series of experimental decompression of rhyolitic and phonolitic melts, totaling 49 individual samples. Published data are from the studies of Gardner and Denis (2004), Gardner (2007), Cluzel et al. (2008), and Shea et al. (2010). In addition, we analyzed three samples of experimentally decompressed rhyolite melts (Burgisser and Gardner, 2004). In their study, Burgisser and Gardner (2004) placed

6

samples of rhyolitic glass in sealed Au-capsules with distilled water at 825 °C and 150 MPa for five days in order to saturate the melt with water. A sudden decompression down to 100 MPa nucleated small bubbles and samples were maintained at the nucleation pressure until bubbles reached approximately thermodynamic equilibrium with a mean diameter of 35 μm. The analyzed sample (ABG1) was quenched at 100 MPa. For the other two samples, pressure was released in increments to approximate a constant decompression rate of 0.5 MPa/s (ABG16) and 1 MPa/s (ABG28) until 50 MPa was reached, at which point the samples were rapidly quenched. For simplicity, the experimentally generated bubbles will sometimes be referred to as vesicles in discussions involving both natural and experimental samples.

2.2 2D imaging

2.2.1 Acquisition

New natural data were collected over several years and quantification methods slightly varied according to sample series. Textural characterization of samples from Soufrière Hills, Mt Pelée, and Lascar volcanoes was done by imaging polished sections by SEM with a JEOL JSM-6400 microscope operating at 15 to 20 kV acceleration voltages (ISTO, Université d'Orléans). BackScattered Electrons (BSE) images were acquired at three to four different resolutions to ensure that a sufficiently wide range of object sizes was represented. Three to four SEM images were acquired at each of the following magnifications: ×25, ×100, ×400, and ×800. One exception is that the ×400 magnification was replaced by ×200 for samples AMO16C and 1448 that were deposited by the Soufrière Hills block-and-ash flows. For the sample series of Merapi volcano, we used the SEM images at two levels of magnification (×50 and ×2000) that have been described in Drignon et al. (2016), where details of the acquisition procedure can be found. The Merapi polished sections were imaged using a TESCAN MIRA 3 XMU SEM operating at 20 to 25 kV accelerating voltage (CNRS-ISTO, Université d'Orléans) in BSE mode.

One sample from Merapi was imaged by Energy Dispersive Spectroscopy (EDS) as reported in Drignon et al. (2016). Briefly, the polished section was imaged using a LEO STEREOSCAN 440 (LEICA) SEM operating at 15 kV accelerating voltage (Université Savoie Mont Blanc) to which an EDS probe QUANTAX EDS (Bruker AXS) was attached. Distribution maps of Si, Fe, Mg, Al, Ca, K, Ti, and C were acquired at three to four locations per magnification. The magnifications used were ×35, ×352, and ×2000 and the resolution of each element map was 512×384 pixels.

2.2.2 Processing

All images were treated using the image processing packages ImageJ 1.48 (imagej.nih.gov/ij/) and Fiji 1.52 (Schindelin et al., 2012). Noise reduction was performed on the SEM images using ImageJ anisotropic diffusion filter. Segmentation of vesicles and oxides was done by manual thresholding of the lowest and highest levels of gray, respectively. Plagioclases are difficult to distinguish from glass, impeding calculation of total crystal volume fractions based on automatic segmentation (Burgisser et al., 2010). For some Soufriere Hills samples and all Merapi samples (Table S1), we used vesicularities and total crystal volume fractions (phenocrysts plus microlite) reported in Drignon et al. (2016) and some crystal volume fractions reported in Burgisser et al. (2010). This is because in both studies, precise segmentation of plagioclases was conducted by manual outlining the plagioclases. In all the other SEM images, we set thresholding values that yielded one segmented phase containing glass, plagioclase, and all other minerals but oxides. We then manually erased the glass from the thresholded image by visual inspection. Unlike the methods of Burgisser et al. (2010) and Drignon et al. (2016), this method does not yield outlines of every crystal, which does not affect the accuracy of area fraction but leads to inaccurate size distributions.

Images acquired by EDS were processed with the wavelet "A-trous" filter in ImageJ to decrease the noise level before using the default IsoData thresholding. Objects of interest were obtained by successive subtractions of Boolean combinations of the binary images (Drignon et al., 2016). Vesicles were composed of pixels containing C or none of the other elements. Oxides were

composed of pixels containing Fe and Ti but no vesicle pixels.

2.2.3 Analysis

For each sample, segmented SEM and EDS images were used to quantify volume fractions and number densities of vesicles, oxides, and other crystals following the resolution assembly procedure of Giachetti et al. (2010). All samples but those of Merapi had similar cut-off values for oxides and vesicles. Images at ×25 magnification were used to characterize objects 1500–8.4 μm across, ×100 images were used to characterize objects 267–2.1 μm across, ×400 images were used to characterize objects 66.8–0.52 μm across, and ×800 images were used to characterize objects 33.6–0.38 μm across. The corresponding cut-off values between these successive magnifications varied between 16 and 100 μm, 4 and 16 μm, and 4 and 0.6 μm, respectively (see Giachetti et al., 2010, for statistical details on image vs. object sizes). Only crystals with an equivalent diameter larger than 50 μm were counted, except for AMO36, for which operator 3 used all four magnifications with the same cut-off values as for oxides and vesicles. For each Merapi sample, we cropped one ×50 image from the native resolution of 2048×2048 pixels to ~1300×1300 pixels because of the circular shape of the polished sections. The cropped image was used to characterize objects 1500–20 μm across. Four ×2000 images were used to characterize objects 63–0.5 μm across with a corresponding cut-off value varying between 30 and 60 μm depending on sample.

Object counting and characterization of each magnification was done using the Analyze Particle tool of ImageJ. Our thresholding of SEM images creates false positives of oxides because of the edge effect at the glass/vesicle interface. In some series where the edge artifacts were strong, we eliminated many such false positives on the basis of their cuspate shapes by filtering out objects with circularity <0.3. Number density and volume fraction of the objects were then obtained by combining the different levels of magnifications as explained in Giachetti et al. (2010). Both ONDs and VNDs are reported (Table S1) on a bubble- and crystal-free basis (i.e. the number of objects per unit volume of

glass). Uncertainties on each number density measurement were calculated according to Giachetti et al. (2010) by assuming that 5% of the number of objects per image were artifacts.

We used the total VNDs and ONDs of the Kilian volcano products reported in Colombier et al. (2017) but adjusted their crystal volume fractions with a combination of XRD analysis and mass balance to calculate bubble- and crystal-free number densities. The SEM image analysis underestimated crystal volume fractions because of the high volume fractions (SI Text 1, Colombier et al., submitted).

2.3 3D imaging

Relationship between oxides and bubbles can be determined in 2D by using statistical analysis of their spatial distribution (Edmonds et al., 2015) but we used the more direct approach of 3D measurements on representative natural and experimental samples. Six samples from the 1997 Vulcanian explosions at Soufrière Hills and three samples of experimentally decompressed rhyolite melts were imaged by Computed micro-Tomography (μCT) to obtain 3D volumes of X-ray attenuation levels.

2.3.1 Acquisition

The X-ray μ-CT acquisition of the experimental samples were performed following the method described in Castro et al. (2012). The 3D volume of ABG1 is the same as that used in Castro et al. (2012) and the volumes of AGB16 and ABG28 are the same as those used in Burgisser et al. (2017). Briefly, scanning was performed with a Phoenix Nanotom 180 (ISTO, Université d'Orléans) with a molybdenum target, a tungsten filament, a variable operating voltage of 100 to 180 keV, and a filament current of 50–210 nA. We analyzed small (1–4 mm^3) chips of vesicular glass by mounting them onto carbon fiber rods with thermoplastic adhesive. Samples were rotated over 360° during the exposure to the X-radiation. Between 1300 and 2300 images of 2304×2304 pixels were collected during each analysis. Reconstruction of these images into a stack of grayscale images representing

10

different phases was performed with a separate PC microcluster running Phoenix reconstruction software. This piece of software includes a proprietary ring artifact correction procedure based on averaging and subtraction of blank images taken during acquisition by temporarily removing the sample from the field of view. The voxel edge length was 2.2 μm for ABG1, 1.9 μm for ABG16, and 1.5 μm for ABG28.

The μ-CT acquisitions of the natural samples were performed at the TOMCAT beamline of the SLS synchrotron facility (Villigen, Switzerland; Stampanoni et al., 2006) following the procedure described in Degruyter et al. (2010). The imaged samples were small volumes of rock immediately adjacent to those forming the polished sections imaged by SEM to minimize the effects of spatial variability. The beam energy was varied between 20 and 25 keV. Samples were rotated over 180° and between 1000 and 3000 projections were taken per scan. A field of view of 5.5×5.5 mm^2 and a resolution of 2048×2048 pixels were used. Reconstructions of the 3D volumes were done using the in-house software developed at the synchrotron beamline, yielding a voxel edge length of 2.7 μm. No ring artifact correction was needed.

2.3.2 Processing

All volumes were treated using ImageJ and Fiji. They were converted to stacks of 8-bit grayscale images, and were then cropped into cuboids for further analysis. Noise reduction was performed on most volumes with the wavelet "A-trous" filter, and with the "anisotropic diffusion" filter on the remaining volumes. The filtered image stacks were converted to binary format by manual thresholding of the highest and lowest levels of gray to segment oxides and vesicles, respectively. Sub-volumes were cropped so that no sample edge was present in the volume of interest (VOI). This yielded VOIs of ~1000^3 voxels for natural samples (Table S2). The small sizes of the experimental samples (Burgisser et al., 2017) constrained us to use VOIs <600^3 voxels. Details on 3D rendering parameters are in Text S2.

11

2.3.3 Analysis

Oxides and vesicles were counted using the "Particle Analyzer" tool of the BoneJ plugin (Doube, 2020) of ImageJ. The minimum size of all objects was set to 10 voxels for natural samples. No scan at higher resolution was available, and the consequences of this lower limit are assessed in section 2.4. The simple texture of the experimental samples allowed us to tailor the minimum size of counted bubbles to 27 voxels. Resulting bubble mean diameters in the analyzed VOIs are 25 μm for ABG1 and 66 μm in ABG 16, which are comparable to the values reported in Burgisser and Gardner (2004): 35±7 and 71±8 μm, respectively.

To test whether the VOIs of the experiments had sufficient resolution to capture the fine end of the oxide size distribution, we used the ABG28 volume because it was acquired at the highest resolution (voxel edge length of 1.5 μm). The three samples were extracted from the same ~100 cm^3 block of obsidian glass and are part of similar decompression series that did not nucleate new crystals (Burgisser and Gardner, 2004). The only source of differences in the size distributions of the three samples is natural variability within the original obsidian glass block. The minimum size of counted oxides was 8 voxels for ABG1 and ABG16. Thanks to a less noisy stack (Fig. S1), oxides in ABG28 were counted with a lower threshold of 4 voxels. Figure 1 shows the resulting size distribution, which can be used to estimate the number of oxides that were too small to be captured by the μCT scan. We carried out this extrapolation by first fitting a power law curve to the fine end of the distribution (15–400 μm^3). We then used this fit (R^2=0.99) to calculate the putative cumulative number of oxides between 15 μm^3 and the single oxide of 0.023 μm^3 predicted by the power law. Results indicate that 152 oxides <15 μm^3 could be present in the ABG28 VOI. As we measured 8553 oxides in that VOI, the number of oxides could thus have been underestimated by 1.7%. Figure 1 also shows the limits of the smallest oxides analyzed in the two other samples. Applying the same reasoning to those samples, our analysis thus captured 83% and 88% of the oxides present in ABG1 and ABG16, respectively. This source of positive uncertainty is larger than the one stemming from calculating the standard

deviation between VOIs of different sizes (see below).

Calculating number densities in 3D is more straightforward than in 2D. The numbers of oxides, N_{ox}, and vesicles, N_{ves}, in the analyzed volumes were divided by the volume of glass (i.e. the total volume minus that of the vesicles and that of the oxides) to obtain ONDs and VNDs, respectively (Table S1). This was done only for the experimental samples because their unimodal bubble size distributions were fully captured within the VOIs. Giachetti et al. (2011) have shown that obtaining accurate ONDs and VNDs in natural samples requires combining stacks of different resolutions and an automated de-coalescence of the connected vesicle network. Such analysis is beyond the scope of our study, and we used their values instead (Table S1).

The level of connectivity between vesicles and oxides is a measure of how many oxides are in close contact with vesicles and vice-versa. In each VOI, oxides were dilated by 1 voxel and counted to obtain the number of dilated oxides, N_{ox-d}. Dilation is necessary because when a voxel contains a vesicle–oxide contact, the contrast in X-Ray attenuation between the mineral and the vesicle yields an average value of attenuation that is segmented in neither phase. The volume containing the dilated oxides was combined with the volume containing the segmented vesicles so that the result is a volume containing segmented objects that are either isolated vesicles, or isolated oxides, or oxide–vesicle pairs. In other words, the Boolean operator *or* was applied between the volume with dilated oxides and that with vesicles. As the uCT scans had similar resolutions, dilation assumes overall that oxides closer than about 2 μm from vesicles are connected to these vesicles. Objects in the resulting volume were counted to obtain the total number of objects, N_{tot}, which comprises isolated vesicles, isolated oxides, and connected oxide(s) and vesicle(s). The number of connected objects was defined as: $N_{conn} = N_{ox-d}+N_{ves}-N_{tot}$. The levels of connectivity of oxides and vesicles are measured by the ratios N_{conn}/N_{ox} and N_{conn}/N_{ves}, respectively. Values >1 mean that each object of the considered phase is connected to several objects of the other phase. Figure S2 illustrates these two measures of connectivity and their limitations. Text S3 details the error propagation of the lower detection limit of

13

oxides on N_{conn}/N_{ox} and N_{conn}/N_{ves}.

To determine whether our VOIs were representative elementary volumes (REVs), we measured levels of connectivity in VOIs of progressively smaller sizes. To reduce computing time, this was done by using an object counting method based on object centroids (see Fig. S3 for details). Figure 2 shows the level of connectivity of oxides, N_{conn}/N_{ox}, measured in a series of volumes of progressively smaller sizes. Volumes with $>10^8$ voxels for natural samples and $>10^7$ voxels for experimental samples are statistically representative because they are above the size at which fluctuations between different volumes stabilize. This difference in minimum REV size is due to the fact that the largest natural vesicles are larger than their experimental counterparts. Figure 2 shows that all the largest VOIs (Table S2) are REVs. We thus report the levels of connectivity measured on the largest VOIs for all samples. We used the standard deviation of the three largest VOIs to estimate uncertainties on the connectivity of natural samples. The minimum error of the experimental samples was also the standard deviation of the three largest VOIs. The maximum error of the experimental samples, however, was that due to the lower detection limit of oxides (Text S3).

In natural samples, because segmentation of glass and other crystals in the μCT volumes is challenging, we opted to use the crystal contents from the SEM analysis. In experimental samples, Fe-Ti oxide is the only mineral phase and is easy to segment.

2.4 Measurement accuracy

The procedure of Giachetti et al. (2010) retrieved vesicle size distributions with great accuracy because it used 6 overlapping levels of magnification and a step of vesicle de-coalescence (i.e. closing manually partially retracted walls between neighboring vesicles) to reconstruct these distributions. This high accuracy was obtained at the expense of a labor-intensive, time-consuming process. One goal of our analysis procedure was time efficiency, which guided the choice of the number of magnifications and that of minimizing manual operations during image analysis. The result of these

14

choices was to maintain the accuracy of the OND and VND determinations at the expense of a loss in the resolution of object size distributions.

Figure 3 shows object number densities for one characteristic pumice sample, AMO36, that were determined using three different segmentation procedures. The first procedure is that of Giachetti et al. (2010), which yields accurate OND and VND that we use as reference values. The second procedure (Giachetti et al., 2011) combined 3D μCT data from multiple image stacks with different spatial resolutions to generate vesicle size distributions. The third procedure is our 4-magnification levels method, which was applied on AMO36 by three different human operators using slightly different combinations of segmentation thresholds and cut-off values between magnifications.

The multiscale 3D data of Giachetti et al. (2011) yield a VND similar to that measured on SEM images, but an OND that is 1.5 log units below that from SEM images (Fig. 3). This has been shown by Giachetti et al. (2011) to be resulting from the comparatively lower resolution of the μCT imaging, which imposes a lower minimum cut-off value (3.4 μm) compared to the SEM image (0.38 μm). The μCT reconstructions thus fail to image the smallest oxides, which are present in high number densities in that sample. The SEM vesicle separation procedure of Giachetti et al. (2011) includes a step of vesicle de-coalescence, whereas ours does not. Figure 3 shows that the absence of de-coalescence does not affect results because the smallest, most numerous vesicles are generally isolated and not subject to de-coalescence. Considering the SEM image magnifications we used, objects larger than 1.5–3 mm across are expected to be missing from our size distributions (Giachetti et al., 2010). This is not an issue for the generally smaller oxides, but it strongly affects vesicle volume distribution as vesicles larger than 1.5 mm occupy up to a quarter of the volume of void (Giachetti et al., 2010). Cumulated number densities, however, are not affected by the upper size limit because large vesicles are far less numerous (10^8–10^{10} m^{-3}) than smaller ones (10^{15}–10^{16} m^{-3}). This is visible in Fig. 3, which shows that the reference size distributions determined by Giachetti et al. (2010) and those obtained with our method yield similar cumulated number densities. All our analyses involve 4 magnification

15

levels, except those of Merapi products and those of the February 2010 Soufrière Hills explosive products that only involve two magnification levels. It has been shown in Drignon et al. (2016) and Burgisser et al. (2019) that cumulated number densities in these samples are unaffected by the artifacts introduced by this information gap because the smallest and most numerous objects are captured by the highest SEM magnification.

Another issue is that oxides have been shown to be very small in products of explosive eruptions, reaching nanolite sizes (Mujin and Nakamura, 2014). Compared with the SEM procedure, the EDS procedure is able to capture smaller oxides because oxides have a chemical composition that is distinct from that of the other minerals. Figure 3 shows that EDS based images of sample AME10G with a cut-off limit of 0.1 μm yield an OND that is 1 log unit *higher* than that of SEM images with a 0.38 μm cut-off. That more oxides are found at a lower cut-off is consistent with the presence of oxide nanolites in our samples. This suggests that our SEM-based ONDs with a 0.38 μm cut-off are minimum values because Mujin and Nakamura (2014) report oxide nanolites of 0.01–0.02 μm. The μCT reconstructions of natural samples underestimate natural ONDs by an additional one order of magnitude. This is not the case for experimental samples because the μCT scans capture 83–98% of the oxides (Fig. 1).

Finally, EDS images with the same 0.38 μm cut-off limit as the SEM images yield an OND that is 1 log unit *lower* than that of SEM images. This counter-intuitive result is due to our thresholding of SEM images, which creates false positives because of vesicle edge effects that a circularity filter limits but does not suppress. The remaining false positives (i.e. bubble edges incorrectly counted as oxides) compensate somewhat the loss caused by the high cut-off value, but do so in a way that is difficult to quantify.

The intrinsic errors of the different methods are much smaller than inter-operator variability (Fig. 3). We thus based the overall uncertainties of our number densities on the maximum differences between the four SEM determinations of Fig. 3, which correspond to ±0.13 log units for oxides and

16

±0.15 log units for vesicles, and we consider our ONDs as minimum values. We applied those two levels of uncertainty due to inter-operator variability to all samples analyzed in 2D, regardless of their origin (new, re-analyzed, or published).

3 Results

3.1 Vesicle types and oxide–vesicle contacts

Vesicles in our natural samples were subdivided in sub-populations using the criteria of Giachetti et al. (2010). There are two main types of small (<30–50 μm) vesicles. The first type, S1, is composed of rounded, isolated vesicles that occur in vesicular samples (Fig. 4A), such as the ones described in Giachetti et al. (2010) and Burgisser et al. (2010). The second type, S2, is composed of irregular voids often delimited by crystal faces that occur in dense samples with a diktytaxitic texture (Fig. 4B). A couple of samples feature both types (Fig. 4C). One sample from Mt. Pelée features deflated vesicle textures such as narrow, pinched-off necks connecting two flattened vesicles (Fig. S4) associated with bubble collapse (e.g., Adams et al., 2006; Moitra et al., 2013; Pistolesi et al., 2015). We did not find in our samples bubble collapse textures linked to shear-bands (Wright and Weinberg, 2009). There are three types of large (>30–50 μm) vesicles. Two of them are composed of deformed vesicles of equivalent size >300 μm across and circularity <0.2. Type L1 comprises large angular voids between crystal fragments that are interpreted to have been formed in response to the decompression accompanying the Vulcanian explosion (Giachetti et al., 2010; Burgisser et al., 2010; Burgisser et al., 2019). Type L2 is composed of the remaining vesicles of >300 μm, which are considered as pre-explosive vesicles. Type L3 is composed of 40–300 μm, lobate vesicles that result from newly nucleated S1 bubbles that have undergone some growth and coalescence (Giachetti et al., 2010).

On the basis of 2D observations, the first small vesicle type S1 has been often associated with

17

oxides (e.g., Giachetti et al., 2010) and represents the latest syn-explosive nucleation event. Here we extend these observations to 3D by looking at the proportion of oxides that are touching S1 vesicles (or in close proximity of <3 μm) and vice-versa. Figure 5 shows the fractions of oxides and vesicles that are in close contact with one another. In natural samples bearing S1 vesicles, the level of oxide–vesicle connectivity ranges from 55% to 100% and the level of vesicle–oxide connectivity ranges from 16% to 72%. In other words, half to all oxides touch vesicles whereas a smaller and more variable proportion of vesicles are in contact with oxides. Figure 6A-B shows 2D and 3D renderings of a representative sample with an oxide–vesicle connectivity of 90% and a vesicle–oxide connectivity of 16%. It illustrates that most oxides are protruding inside vesicles whereas most vesicles contain no oxides.

Because it is the hallmark feature of the diktytaxitic texture, S2 vesicles are mostly observed in samples with that texture, although we observe a continuum between the proportions (and shapes) of S1 and S2 vesicles in our samples (Fig. 4). We note that none of the classical shape indicators such as circularity, elongation, or shape factor Ω (Mitra et al., 2013) could reliably discriminate the two vesicle types in 2D images. Although in contact with oxides (16% of the vesicles of the diktytaxitic sample of Fig. 5 touch oxides), S2 vesicles are mostly found in low-porosity dome samples and block-and-ash flow products. One likely origin of these vesicles is reorganization of voids under shear (Laumonier et al., 2011). Here we simply assume that the number density of S2 vesicles is not caused by nucleation and that there is thus no genetic link between oxides and S2 vesicles. This leads us to consider block-and-ash flow products separately from those issued from ash fallout or fountain collapse.

The decompression experiments of Burgisser and Gardner (2004), which involve rhyolitic melt bearing <0.1 vol.% oxides, provide additional constraints on the relationship between bubbles and oxides. Figure 5 indicates that ~100% of the bubbles are in contact with an oxide in ABG1. In the two other samples, 155–215% of the bubbles are in contact with an oxide, which means that bubbles

touch, on average, 1.6–2.2 oxides. This connectivity increase is most likely due to bubble growth because bubble size goes from 25 μm in ABG1 at a quench pressure of 100 MPa to 56–66 μm in ABG16 and ABG28, which were both quenched at 50 MPa (Burgisser and Gardner, 2004). Conversely, 64% to 88% of the oxides touch experimental bubbles, indicating a high level of connectivity (Fig. 6C). As shown below, these levels of connectivity are consistent with the comparable VND and OND values of this experimental series.

3.2 Vesicle and oxide number densities

Figure 7 shows vesicle and oxide number densities of all our samples plus samples from the literature. Figure 7A indicates that the nearly aphyric glasses from experiments have number densities spanning from 10^{10} to 10^{16} m^{-3}. Samples in Fig. 7A can be divided into three categories: samples featuring more oxides than bubbles such as the series of Cluzel et al. (2008) and Shea et al. (2010), samples with more bubbles than oxides such as the series of Gardner (2007) and most samples of Gardner and Denis (2004), and samples with bubbles and oxides in equivalent numbers such as those of Burgisser and Gardner (2004).

Natural samples were divided into two categories according to the dominant texture present in the samples from individual eruptive events. The first category (Fig. 7B) is mostly composed of vesicular pumice clasts from eruptions dominated by explosions with a strong vertical component (Vulcanian events at Soufrière Hills, Lascar, and Kilian volcanoes, sub-Plinian and blasts events at Merapi and Mount St. Helens volcanoes). The second category (Fig. 7C) is mostly composed of dense pumice clasts with diktytaxitic and intermediate, vesicular–diktytaxitic textures from dome collapse events (Soufrière Hills and Mt Pelée volcanoes) and lateral blast (Mt. Pelée volcano). Overall, number densities in natural samples are higher than those in experimental samples. Pumice clasts from vertical explosions have a wide OND range, spanning 10^{14} to 10^{17} m^{-3} and a VND range that clusters around 10^{15} to 10^{16} m^{-3} (Fig. 7B). As we assume no genetic link between oxides and S2 vesicles, we only

19

report OND of diktytaxitic samples. The sample from the 1980 Mount St. Helens blast appears to be an outlier with low OND, which is likely due to the abundance of microlites that are too small to be detected (Cashman, 1988), and will not be considered further in our analysis. Figure 7C suggests that ONDs from dome collapse events are similar (within about one order of magnitude) to those from explosive events at the same volcano. The two samples from the 1929 block-and-ash flow at Mt Pelée are noteworthy. One sample is a pumice clast with 36 vol% vesicles that are rounded, which is a texture that is commonly found in most vesicular products of block-and-ash flows. The OND and VND of this sample are almost identical. The second sample is a dense clast with 12 vol% vesicles that have a deflated texture with concave shapes, which is commonly interpreted as having resulted from outgassing and gas escape. For this sample, we considered that the collapsed vesicles were not directly linked genetically to oxides because coalescence and collapse modify number densities, and only reported the OND (5×10^{14} m^{-3}), which is close to that of the more vesicular pumice (1.3×10^{15} m^{-3}).

For some explosive events at Soufrière Hills, Kilian, and Merapi volcanoes, water content analyses have been used to retrieve pre-explosive values of porosity and pressure of the analyzed samples (Drignon et al., 2016; Colombier et al., 2017; Burgisser et al., 2019). Although magma can rise in the conduit prior to a Vulcanian explosion in a step-wise fashion (Druitt et al., 2002; Jaquet et al., 2006; Clarke et al., 2007; Mann et al., 2013), we tested here the simpler view that oxide microlite nucleate and grow between the moment magma leaves the reservoir and the moment it reaches its pre-explosive position. Phase equilibria experiments have constrained the main storage pressure to ~130 MPa at Soufrière Hills (Barclay et al., 1998) and to ~350 MPa at Kilian (Martel et al., 2013). Estimating reservoir pressure at Merapi is a complex task because the magmas feeding the 2010 eruption were stored at multiple levels and mixed prior to their final ascent towards the surface (Costa et al., 2013; Nadeau et al., 2013; Preece et al., 2014; Erdmann et al., 2016; Widiyantoro et al., 2018). Here we follow Drignon et al. (2016) and assume a storage pressure of 300 MPa so that it is slightly

20

higher than the deepest conduit storage pressure of our samples while being compatible with the location of the main reservoir region (Widiyantoro et al., 2018). Figure 8 shows OND as a function of the pressure difference between the reservoir and the pre-explosive storage location in the conduit. There is no relationship between OND and reservoir–conduit pressure difference for the Merapi events. At Soufrière Hills and at Kilian (notwithstanding the limited data), these two parameters are positively correlated. The choice of the reservoir pressure does not influence these trends.

There is textural evidence that our VNDs track small bubbles nucleated during the explosion when magma leaves its pre-explosive location to be expelled into the atmosphere. At Soufrière Hills, Giachetti et al. (2010) and Burgisser et al. (2019) have shown that S1 and L3 vesicles, which are mostly responsible for the VND values in non-diktytaxitic samples, were formed in response to the decompression accompanying the Vulcanian explosions. More than half (and often more than 80%) of the oxides touch vesicles (Figs. 5 and 6A-B). In addition, wetting angles between oxides and vesicle (Giachetti et al., 2010) are compatible with those that have been determined experimentally (Hurwitz and Navon, 1994). These lines of evidence suggest that oxides were nucleation sites for the syn-explosive vesicles. Although our measurements indicate vesicle–oxide connectivity of up to 90%, in most cases only 15–40% of the vesicles touch oxides (Fig. 5), indicating large numbers of orphaned vesicles and highlighting the many transformations affecting magma during ascent and subsequent evacuation. Pre-existing L2 vesicles, for instance, are not expected to be in contact with oxides because they nucleated before the oxide microlites. These crystal-rich magmas (the median vesicle-free crystal content is 45 vol.%, Table S1) have limited interstitial space in which syn-explosive bubble growth and coalescence can occur, which changes bubble–oxide association. These transformations make it unlikely that the near linear relationship between VND and OND for the Merapi eruption (Fig. 7B) is fortuitous. We suggest instead that the VND is often 0.5 order of magnitude below the OND because some S1 syn-explosive bubbles underwent coalescence, thereby expanding the coarser syn-explosive population and lowering VNDs. This offset could even be an underestimate because

21

ONDs represent minimum values. The more complex case of Soufrière Hills is discussed in section 4.2.1.

That VNDs are controlled by the sudden decompression accompanying conduit evacuation allows us to determine decompression rate at both Merapi and Soufrière Hills. When oxides are at least as numerous as vesicles in a given volume (Fig. 7A), Cluzel et al. (2008) have shown that the decompression rate needed to generate the observed VND can be calculated using the simplified nucleation model of Toramaru (2006). The 2010 Soufrière Hills samples were thus removed from this analysis because they have more vesicles than oxides (Fig. 7B). Pressures shown in Fig. 8 were calculated using the water solubility relationship of Liu et al. (2005). To circumvent the disadvantage that this relationship is not invertible while maintaining self-consistency, we calculated the values of constants, a and b, by fitting the relationship of Liu et al. (2005) with the following solubility relationship relating pressure in MPa, P, to melt water content in wt%, C:

$$C = aP^b \tag{1}$$

The calculated values (a=0.3293 and b=0.5343 for Soufrière Hills and a=0.3054 and b=0.5402 for Merapi) recover the relationship of Liu et al. (2005) over the pressure range of interest. Following Cluzel et al. (2008), we assumed a water diffusivity of 10^{-11} m^2/s, a molecular volume of water in the melt of 3×10^{-29} m^3, and a water-magnetite effective surface tension of 0.025 N/m. Temperature and melt densities of 850 °C and 2450 kg/m^3 were used for Soufrière Hills (Barclay et al., 1998; Burgisser et al., 2010). Corresponding values for Merapi were 930 °C and 2455 kg/m^3 (Costa et al., 2013; Erdmann et al., 2016). Figure 9 shows the resulting decompression rates alongside those at Kilian, which were obtained by Colombier et al. (2017) using a similar approach. The events at the three volcanoes yield similar rates of 3–30 MPa/s, regardless of sample position in the conduit.

22

4 Discussion

4.1 Experimental samples

The three categories of experimental samples (Fig. 7A) are consistent with the conclusions of the respective experimental studies. Studies featuring more oxides than bubbles report agreement between VND and nucleation models (e.g., Toramaru, 1995; Toramaru, 2006) that are mainly controlled by supersaturation, water diffusivity, melt viscosity, and decompression rate (Cluzel et al., 2008; Shea et al., 2010). Studies featuring more bubbles than oxides report little agreement with such models (Gardner, 2007; Gardner and Denis, 2004). Among the possible reasons proposed in those works for such mismatch, one is consistent with Fig. 7A: "*[VND] is relatively constant in MCR rhyolite, and probably reflects the number of sites for nucleation on magnetite (and the few ends of hematite) that can potentially be used*" (Gardner, 2007). The study with bubbles and oxides in equivalent numbers (Burgisser and Gardner, 2004) reports remarkably consistent VNDs between experiments having undergone a manual pressure drop from 155 to 100 MPa in <1 s. Our 3D analysis reveals that nearly all oxides in these samples have a bubble attached to them, and all bubbles are connected to one or two oxides, suggesting that bubble nucleation continued until all the sites offered by the oxides were used. Revisiting other experimental work addressing bubble growth (e.g., Cichy et al., 2011; Fiege and Cichy, 2015) by measuring ONDs might thus show that oxide-controlled bubble nucleation is more pervasive than currently thought.

These results suggest a simple, testable hypothesis to assess the likelihood of heterogeneous bubble nucleation. If, given a set of decompression conditions (melt composition, decompression rate, etc.) in a bubble-free, oxide-bearing melt, the OND is higher or equal to the VND predicted by heterogeneous nucleation models, the final number of nucleated bubbles will be consistent with model predictions. Conversely, if the decompression conditions are such that the VND predicted by heterogeneous nucleation models is higher than the OND, the final number of nucleated bubbles

cannot be predicted accurately. Figure 7A hints that the OND could act as an upper limit to VND up to a certain degree of supersaturation above which nucleation is able to produce more bubbles than the number of available oxides. This has important implications for the interpretation of natural samples, which are explored in the next section.

One piece of evidence supporting that hypothesis can be found in the series of heating and decompression experiments from Pleše et al. (2018), Pleše et al. (2019a), and Pleše et al. (2019b). These studies report heterogeneous bubble nucleation in andesitic melts seeded with plagioclase, clinopyroxene, and oxides. Nucleation occurred first on plagioclase and/or clinopyroxene and, surprisingly, last on oxides. The melt-referenced OND of these samples ranges from 3.3×10^{10} to 1.3×10^{12} m^{-3} assuming a crystal content of 30 vol% for all samples (Pleše et al., 2018). The VND is not reported in the heating experiments of Pleše et al. (2018) because of segmentation issues (P. Pleše, pers. comm. 2019). Using the reported bubble and sample volumes and assuming an average bubble size of 10 to 100 μm based on the μCT images, our rough estimate of the melt-referenced VND is $3 \times 10^{11} - 7 \times 10^{15}$ m^{-3}. Using the reported bulk VND in pure melt regions and assuming an average porosity of 10–20 vol% based on the μCT images, our rough estimate of the melt-referenced VND in the decompression experiments of Pleše et al. (2019a) is $8 \times 10^{12} - 8 \times 10^{14}$ m^{-3}. In both series, every sample has a VND that is always larger than its OND, suggesting that oxides were present in insufficient numbers to provide monomineral nucleation sites for the bubbles. Nucleation was thus prone to occur on the other phases that were present. This interpretation does not undermine the finding that plagioclase with rough surfaces have better nucleation properties than previously envisioned (Pleše et al., 2018). Instead, it provides an alternate explanation of why oxides were the last occupied nucleation sites in both experimental series.

4.2 Natural cases

Fe–Ti oxides are subject to fast re-equilibration during decompression because of cooling,

24

changes in redox state and melt water loss (e.g., Andersen and Lindsley, 1988; Venezky and Rutherford, 1999; Devine et al., 2003; Ghiorso and Evans, 2008). Although the decompression threshold for bubble nucleation is lower for magnetite than, for instance, hematite (Cluzel et al., 2008), the end-members of the solid solution are not separated in our data. This warrants further investigation by using, for instance, element mapping (Muir et al., 2012; Drignon et al., 2016) instead of SEM imaging to distinguish between the ONDs of hematite, ilmenite, and magnetite. For simplicity, in the following discussion, we ignore that several bubbles can nucleate on the same crystal, increasing the final VND by at most 0.5 order of magnitude (Gardner and Denis, 2004; Edmonds et al., 2015), and that other phases can cause heterogeneous nucleation, which also increases the VND (Hurwitz and Navon, 1994; Pleše et al., 2018). We also keep in mind that ONDs are minimum values because our analysis cannot identify nanolites that are <380 nm.

Despite these limitations, the observation that the VNDs at Soufrière Hills, Kilian, and Merapi result from a narrow range of high decompression rates regardless of pre-explosive storage pressure (Fig. 9) is compatible with the 0.1–10 MPa/s propagation rate of the fragmentation front given by conduit flow model simulations of short-lived Vulcanian eruptions at Soufrière Hills (Mason et al., 2006). The fragmentation front that disrupts the magma column and feeds the explosion is accompanied by a decompression front that either is collocated with that fragmentation front, or propagates downward into the part of the conduit that is still intact (Burgisser et al., 2011). Combined with the presence of syn-explosive vesicles and high levels of oxide–vesicle connectivity, Fig. 9 suggests that such decompression front is responsible for syn-explosive bubble nucleation in these Vulcanian and sub-Plinian events. The new bubbles and the associated expansion favor fragmentation, regardless of whether decompression is collocated with fragmentation. Further interpretation of these rates is not easy because the conversion from decompression rate to fragmentation speed depends on the fragmentation mechanism (Toramaru, 2006; Burgisser et al., 2011; Miwa and Geshi, 2012) and on the magma physical properties (Alatorre-Ibargüengoitia et al., 2011; Richard et al., 2013). This result,

however, allows us to posit that a minimum OND is needed in the conduit for the decompression front to nucleate bubbles. Conversely, if oxides are too sparse, the front does not create enough bubbles and magma expansion stops, which is likely to end explosive conduit evacuation. The first-order consequence of this conjecture is that conditions for nucleation were adverse at great depths at Soufrière Hills (<50 MPa above the reservoir, Fig. 8) but were propitious at all depths at Merapi. This partly explains the much deeper evacuation at Merapi. In the next section, we bring together pieces of evidence that support the hypothesis that transition from effusive to explosive eruptions is controlled by the absence or presence of oxide microlites in the conduit, respectively.

4.2.1 Oxides as controls of the effusive–explosive transition

Oxide equilibria conditions are much better known than their nucleation behavior in reaction to decompression. If a mineral phase has reached saturation, whether precipitation occurs by nucleation or by growth depends on the instantaneous level of disequilibrium (e.g., Hammer, 2008; Andrews and Befus, 2020). When ascent conditions are smooth (i.e. devoid of stalling or acceleration), larger disequilibrium levels are easier to achieve at shallow depth. It is thus possible to relate the largest microlites to the deepest levels of nucleation, whereas more numerous, smaller microlites and nanolites appear at shallow levels (Melnik et al., 2011).

The Toramaru et al. (2008) nucleation model relates OND to ascent rate as a function of the initial conditions (pressure and melt water content) for microlite nucleation. This model was used by Murch and Cole (2019) on the Soufrière Hills plagioclase microlite with a modest level of success. Their results highlighted that model validity is restricted to nucleation-dominated decompression conditions, which are unlikely to be fulfilled in the case of lava dome samples that have undergone complex ascent paths with stalling and/or accelerations. With this limitation in mind, in the next part of this section, we determine the most likely depth of nucleation-dominated appearance of oxides at both Soufrière Hills and Merapi, and then use the model of Toramaru et al. (2008) to deduce ascent rates from our ONDs.

26

The ONDs at Merapi volcano cluster around 10^{16}–10^{17} m^{-3}, regardless of the conduit–reservoir pressure (Fig. 8). This suggests that oxide microlites nucleated early in the ascent process, which is expected because oxide phenocrysts were present in the reservoir (Costa et al., 2013; Preece et al., 2014; Erdmann et al., 2016). The positive relationship between OND and reservoir–conduit pressure difference at Soufrière Hills suggests instead that oxide microlite nucleated continuously during ascent. This is consistent with nucleation of oxide, clinopyroxene, and plagioclase during experimental decompression of magmas having the composition of the most evolved groundmass of Soufrière Hills dome products (Couch et al., 2003).

The derivative, dϕ/dP, of the equilibrium crystal volume fraction ϕ, with respect to pressure, P, is a measure of how much a parcel of magma is prone to nucleation. To take feldspar crystallization in the Soufrière Hills magma as a proof of principle, rhyolite-MELTS 1.2 (Gualda et al., 2012, detailed initial conditions are given in Supplementary Text S4) predicts a power law increase of plagioclase volume fraction with decreasing pressure that starts at ~70 MPa. This is compatible with the inference that the most abundant plagioclase microlites appear at ~6–10 MPa (Clarke et al., 2007; Murch and Cole, 2019). Here we use dϕ/dP to determine the origin of the most abundant oxides at both Soufrière Hills and Merapi.

The magmas feeding the 2010 Merapi eruption were stored at various levels before being assembled and erupted. We now refine the single storage pressure used to build Fig. 8 by considering the three starting conditions proposed by Erdmann et al. (2016) for the rhyolite-MELTS decompression. The deep reservoir and the recharge magma decompressions are thus starting at 200 MPa (Supplementary Text S4). Shallow reservoir decompression starts at 100 MPa, even if pre-explosive conduit storage pressures larger than those values were reported by Drignon et al. (2016) and in Fig. 8. The initial conditions of the rhyolite-MELTS decompression of Soufrière Hills magma are the same as for Fig. 8 (Supplementary Text S4).

Figure 10 shows the volume fraction of crystals produced/dissolved per unit of pressure as a

function of pressure for Fe–Ti oxide phases in the Soufrière Hills and Merapi melts. It suggests that the transition from (no) growth to nucleation occurs in the Soufrière Hills conduit at ~20 MPa for magnetite and ~50 MPa for ilmenite. Magnetite nucleation at Merapi is expected to occur at ~10, ~100, or ~200 MPa, depending on the host magma. These calculated stability domains are compatible with the observed oxide compositions at both volcanoes (Supplementary Text S4; Devine et al., 2003; Costa et al., 2013). The resulting nucleation pressures can thus be used as an input into the Toramaru et al. (2008) decompression meter to determine ascent rates.

We calculated ascent rates for each sample with the Toramaru et al. (2008) model using the OND of that sample and the nucleation pressures and corresponding melt water contents deduced from Fig. 10 (Supplementary Text S5). Figure 11 shows the frequency distribution of ascent rates at both Soufrière Hills and Merapi. Overall, Fig. 11 suggests that ascent rates on the order of 0.005–20 m/s were necessary to produce the observed ONDs. A similarly wide range of ascent rates is obtained if, instead of considering one OND per sample, one uses the typical spread of ONDs in the microlite size range found in the eruptive products (Figs. S5–7). The main control of these rates is the nucleation depth, which is particularly noticeable in the case of Merapi (Fig. 11B) owing to the very different origin depths between the three erupted magmas.

Keeping in mind that our estimates are average rates between the nucleation depth and the pre-explosive location, whereas magma ascent is a dynamic process, the rates of Fig. 11 greatly overlap with the critical ascent rate range of 0.005–0.25 m/s for the effusive–explosive transition compiled by Cassidy et al. (2018) who included Soufrière Hills in their compilation. This overlap is not a consequence of shared methodologies because the ascent rates in Cassidy et al. (2018) were estimated using methods that are independent from the oxide microlite decompression meter of Toramaru et al. (2008). Effusive activity is thus far more likely to occur at rates <0.005 m/s, which coincide with rates at which oxide nucleation is unlikely to happen in the conduit. A corollary prediction is that lava dome eruptions have small ONDs at depth.

28

A robust test of the hypothesis that the effusive–explosive transition is controlled by the distribution of OND in the conduit would be to measure the OND of a deep sample of an effusive eruption. Unfortunately, as shown by Fig. 7C, lava dome samples have all reached near-surface conditions where numerous oxides can nucleate in response to cooling, making the formal verification of this hypothesis difficult. There is, however, indirect experimental evidence that oxides do not nucleate at depth during effusive eruptions. Considering that the Soufrière Hills magma contains oxide phenocrysts inherited from the reservoir (e.g., Devine et al., 2003), Martel and Schmidt (2003) have shown that slow decompression from reservoir level to 50 MPa in more than 5–15 days (<0.003–0.009 m/s) causes oxide crystallization to occur by growth instead of nucleation. A conduit filled with slowly rising magma will thus contain the oxide cargo inherited from the reservoir, which is not numerous enough (OND<10^{11} m^{-3}, Figs. S5–7) to act as systematic bubble nucleation sites. Even if other Fe-bearing minerals are present, only large (>20 MPa) pressure fluctuations could trigger heterogeneous nucleation in such a conduit. If, on the other hand, the magma rises fast enough to reach the range of ascent rates at which transitional and pulsatory effusive and explosive activities are likely, the local decompression rates are also sufficient to yield the high ONDs observed in the conduit. Enough new oxides will be added to the crystal cargo for the magma to nucleate bubbles when pressure fluctuations are as small as 5–20 MPa/s.

It is thus not accidental that the critical ascent rates at which transitional effusive and explosive activities occur overlap those at which new oxides are nucleated in the conduit. Oxide microlites are a primer for explosive behavior (Cáceres et al., 2020) because they considerably lower the threshold of pressure changes needed for heterogeneous bubble nucleation (Shea et al., 2010). This strongly supports the conjecture that the OND has to be above a given threshold for the decompression front (section 4.2) to nucleate bubbles. Conversely, it also suggests that if insufficient amounts of oxides are present in a given part of the conduit, no bubbles will nucleate when the decompression front arrives. The resulting lack of bubble-rich magma ready to expand (Burgisser et al., 2011) stops the explosion

from propagating downward, aborting it. One exception to the latter scenario is if the burden evacuated is large enough to foster homogeneous nucleation and rapid gas expansion, such as in the case of a cryptodome suddenly exposed to atmospheric pressure (e.g., Mount St. Helens in 1980).

Overall, this reasoning gives a new meaning to the critical range of ascent rates observed by Cassidy et al. (2018); the critical range is defined by the rates at which oxides nucleate in the conduit. We thus propose that the presence of oxides at depth is a major control of the effusive to explosive transition.

Here we explore two consequences of the posited relationship between OND and explosivity. First, the 2010 Soufrière Hills explosion features near constant VNDs regardless of the OND. This could be partly due to heterogeneous nucleation on other phases such as pyroxenes, or to the presence of nanolites. This is also reminiscent of the experiments with VND>OND, in which a similar saturation density occurs (Fig. 7A). Leaving nanolites aside, this suggests that the decompression magnitude was too high for the number of oxides present and that bubble nucleation was more erratic because it depended on a poorly understood and spatially heterogeneous combination of available nucleation sites, decompression magnitude, and decompression rate (Gardner, 2007). Our interpretation of the Pleše et al. (2018) experiments suggests that syn-explosive bubbles nucleated on the other minerals because oxides were not numerous enough to provide monomineral nucleation sites. This implies that oxides were the last occupied nucleation sites in that Vulcanian event.

The second consequence bears on the interpretation of older eruptions for which no observation such as dome growth rate is available but for which pre-eruptive conditions are known. This is the case of the 9.4 ka BP Vulcanian eruption of Kilian volcano (Martel et al., 2013; Colombier et al., 2017; Colombier et al., submitted). Its trachytic composition differs strongly from the more calc-alkaline magmas of Soufrière Hills and Merapi. As a result, oxides nucleate at 20–50 MPa (Fig. 12A). Figure 12B shows that the measured ONDs resulted from ascent rates lying in the 0.01–1 m/s range, which is within that of the critical ascent rates compiled by Cassidy et al. (2018). It also implies that

below $\sim 7 \times 10^{-3}$ m/s no magnetite microlite would crystallize in the conduit before reaching the cooling dome, making this ascent rate the minimum threshold value for the transition between effusive and explosive behavior.

5 Conclusions

We used new, re-analyzed, and published data to build a compilation of oxide number densities (ONDs) and vesicle number densities (VNDs) of samples from explosive and effusive products at five volcanoes, totaling 76 new determinations and 31 determinations from the literature. Natural samples were from products of Vulcanian explosions at Soufrière Hills, Lascar, and Kilian volcanoes, of laterally directed blasts at Mt Pelée, Mount St. Helens, and Merapi volcanoes, of a sub-Plinian event at Merapi volcano, and of lava dome effusion with intermittent collapse at Soufrière Hills and Mt Pelée volcanoes.

Natural samples were separated into two groups according to the dominant texture present in the samples from individual eruptive events. The first group is mostly composed of vesicular pumice clasts from eruptions dominated by explosions with a strong vertical component (Vulcanian events at Soufrière Hills, Lascar, and Kilian volcanoes, sub-Plinian and blasts events at Merapi and Mount St. Helens volcanoes). Samples from that category are either distributed within 0.5 log unit of the 1:1 trend between VND and OND that spans from 10^{15} to 10^{17} m^{-3}, or have a constant VND of 10^{16}–$10^{16.5}$ m^{-3} regardless of OND. A large proportion of oxides (55–100%) touch vesicles whereas a more variable proportion of vesicles (16–72%) are in contact with oxides.

The second group is mostly composed of dense pumice clasts with diktytaxitic and intermediate, vesicular–diktytaxitic textures from dome collapse event (Soufrière Hills and Mt Pelée volcanoes) and lateral blast (Mt. Pelée volcano). Samples from that category have ONDs in the same broad range as their more explosive counterparts. Their VNDs were not measured because their diktytaxitic textures suggest that vesicles are gaps between crystals with no genetic link to oxides.

31

We compiled new and published data of ONDs and VNDs of five series of experimental decompression of rhyolitic and phonolitic melts, totaling 3 new samples and 46 samples from the literature. Number density data suggest that samples can be divided into three categories: those featuring more oxides than bubbles, those with more bubbles than oxides, and those with bubbles and oxides in equivalent numbers. In this last category, experimental bubbles touch, on average, 1.6–2.2 oxides (i.e. most bubbles are in contact with two oxides whereas the other bubbles are either isolated or touching one oxide) while 64–88% of the oxides are in contact with bubbles. These high levels of connectivity suggest that the role of oxides in controlling bubble nucleation in these decompression experiments has been underestimated. When oxides are at least as numerous as vesicles in a given volume (i.e. when OND>VND), heterogeneous nucleation models (e.g., Toramaru, 1995; Toramaru, 2006) are able to reproduce the nucleation density of vesicles as a function of supersaturation, water diffusivity, melt viscosity, and decompression rate. When oxides are less abundant than nucleated vesicles at the final pressure (i.e. when OND<VND), these models are unable to reproduce experimental data. In that case, comparatively much larger supersaturation pressures are needed to achieve the same VND as when OND>VND.

Building on the textural evidence that VNDs track small bubbles nucleated during conduit evacuation, we calculated the decompression rates responsible for the VNDs at both Merapi and Soufrière Hills. They fall within the same range as those at Kilian volcano (3–30 MPa/s), and are compatible with the fragmentation front propagation rates given by conduit flow model simulations at Soufrière Hills (Mason et al., 2006). Combined with the presence of syn-explosive vesicles and high levels of oxide–vesicle connectivity, this suggests that the decompression front accompanying these Vulcanian and sub-Plinian explosions is responsible for syn-explosive bubble nucleation. This result allows us to posit that a minimum OND is needed in the conduit for the decompression front to nucleate bubbles. Conversely, if there are not enough oxides, the front does not create enough bubbles and magma expansion stops, bringing explosive conduit evacuation to an end.

We used rhyolite-MELTS and the Toramaru et al. (2008) nucleation model to calculate the average ascent rates necessary to yield the observed ONDs at Soufrière Hills and Merapi volcanoes. The resulting rates, 0.005–20 m/s, greatly overlap with the range of critical ascent rate inferred for the effusive–explosive transition (Cassidy et al., 2018). This overlap is not fortuitous; oxides nucleated in the conduit have been proposed to be a primer for explosive behavior (Cáceres et al., 2020) because they require a very small pressure drop for heterogeneous bubble nucleation to occur. Our results thus suggest that a conduit filled with slowly rising magma will only contain the oxide cargo inherited from the reservoir. In the cases included in this study, this cargo was not numerous enough (OND<10^{11} m^{-3}) to act as systematic bubble nucleation sites. Even if other Fe-bearing minerals are present, only large (>20 MPa) pressure fluctuations could trigger heterogeneous nucleation in such a conduit. If, on the other hand, the magma rises fast enough to reach rates at which the effusive–explosive transition is likely, our results show that the local decompression rates are also sufficient to yield the high ONDs observed in the conduit. Sufficient quantities of oxide microlites have then crystallized for the magma to nucleate bubbles when small pressure fluctuations occur.

We thus propose that the presence of oxide at depth is a major control of the effusive to explosive transition. The OND has to be above a given threshold so that the decompression front accompanying magma disruption and evacuation nucleates bubbles. Conversely, if, in a given part of the conduit, insufficient oxides are present, then bubbles do not nucleate even when the fragmentation front arrives. Applied to the older eruption of Kilian, our results suggest that ~7×10^{-3} m/s is the minimum threshold value of ascent rate for the transition between effusive and explosive behavior at that volcano.

Acknowledgments

References

Adams, N.K., Houghton, B.F., Hildreth, W., 2006. Abrupt transitions during sustained explosive eruptions: examples from the 1912 eruption of Novarupta, Alaska. Bull. Volcanol. 69, 189–206. https://doi.org/10.1007/s00445-006-0067-4

Alatorre-Ibargüengoitia, M.A., Scheu, B., Dingwell, D.B., 2011. Influence of the fragmentation process on the dynamics of Vulcanian eruptions: An experimental approach. Earth Planet. Sci. Lett. 302, 51–59. https://doi.org/10.1016/j.epsl.2010.11.045

Andersen, D.J., Lindsley, D.H., 1988. Internally consistent solution models for Fe-Mg-Mn-Ti oxides; Fe-Ti oxides. Am. Mineral. 73, 714–726.

Andrews, B.J., Befus, K.S., 2020. Supersaturation Nucleation and Growth of Plagioclase: a numerical model of decompression-induced crystallization. Contrib. Mineral. Petrol. 175, 23. https://doi.org/10.1007/s00410-020-1660-9

Barclay, J., Rutherford, M.J., Carroll, M.R., Murphy, M.D., Devine, J.D., Gardner, J., Sparks, R.S.J., 1998. Experimental phase equilibria constraints on pre-eruptive storage conditions of the Soufriere Hills magma. Geophys. Res. Lett. 25, 3437–3440.

Burgisser, A., Arbaret, L., Druitt, T.H., Giachetti, T., 2011. Pre-explosive conduit conditions of the 1997 Vulcanian explosions at Soufrière Hills Volcano, Montserrat: II. Overpressure and depth distributions. J. Volcanol. Geotherm. Res. 199, 193–205.

Burgisser, A., Bechon, T., Chevalier, L., Collombet, M., Arbaret, L., Forien, M., 2019. Conduit processes during the February 11, 2010 Vulcanian eruption of Soufrière Hills, Montserrat. J. Volcanol. Geotherm. Res. 373, 23–35. https://doi.org/10.1016/j.jvolgeores.2019.01.020

Burgisser, A., Chevalier, L., Gardner, J.E., Castro, J.M., 2017. The percolation threshold and permeability evolution of ascending magmas. Earth Planet. Sci. Lett. 470, 37–47. https://doi.org/10.1016/j.epsl.2017.04.023

Burgisser, A., Gardner, J.E., 2004. Experimental constraints on degassing and permeability in volcanic conduit flow. Bull. Volcanol. 67, 42–56. https://doi.org/10.1007/s00445-004-0359-5

Burgisser, A., Poussineau, S., Arbaret, L., Druitt, T.H., Giachetti, T., Bourdier, J.-L., 2010. Pre-explosive conduit conditions of the 1997 Vulcanian explosions at Soufrière Hills Volcano, Montserrat: I. Pressure and vesicularity distributions. J. Volcanol. Geotherm. Res. 194, 27–41. https://doi.org/10.1016/j.jvolgeores.2010.04.008

Cáceres, F., Wadsworth, F.B., Scheu, B., Colombier, M., Madonna, C., Cimarelli, C., Hess, K.-U., Kaliwoda, M., Ruthensteiner, B., Dingwell, D.B., 2020. Can nanolites enhance eruption explosivity? Geology. https://doi.org/10.1130/G47317.1

Cashman, K.V., 1988. Crystallization of Mount St. Helens 1980-1986 dacite: A quantitative textural approach. Bull. Volcanol. 50, 194–209.

Cassidy, M., Manga, M., Cashman, K., Bachmann, O., 2018. Controls on explosive-effusive volcanic eruption styles. Nat. Commun. 9, 2839. https://doi.org/10.1038/s41467-018-05293-3

Castro, J.M., Burgisser, A., Schipper, C.I., Mancini, S., 2012. Mechanisms of bubble coalescence in silicic magmas. Bull. Volcanol. 74, 2339–2352. https://doi.org/10.1007/s00445-012-0666-1

Cichy, S.B., Botcharnikov, R.E., Holtz, F., Behrens, H., 2011. Vesiculation and Microlite Crystallization Induced by Decompression: a Case Study of the 1991-1995 Mt Unzen Eruption (Japan). J. Petrol. 52, 1469–1492. https://doi.org/10.1093/petrology/egq072

Clarke, A.B., Stephens, S., Teasdale, R., Sparks, R.S.J., Diller, K., 2007. Petrologic constraints on the decompression history of magma prior to Vulcanian explosions at the Soufrière Hills volcano, Montserrat. J. Volcanol. Geotherm. Res. 161, 261–274. https://doi.org/10.1016/j.jvolgeores.2006.11.007

Cluzel, N., Laporte, D., Provost, A., Kannewischer, I., 2008. Kinetics of heterogeneous bubble nucleation in rhyolitic melts: implications for the number density of bubbles in volcanic

conduits and for pumice textures. Contrib. Mineral. Petrol. 156, 745–763. https://doi.org/10.1007/s00410-008-0313-1

Colombier, M., Gurioli, L., H. Druitt, T., Shea, T., Boivin, P., Miallier, D., Cluzel, N., 2017. Textural evolution of magma during the 9.4-ka trachytic explosive eruption at Kilian Volcano, Chaîne des Puys, France. Bull. Volcanol. 79. https://doi.org/10.1007/s00445-017-1099-7

Colombier, M., Shea, T., Burgisser, A., Druitt, T.H., Gurioli, L., Mueller, D., Cáceres, F., Hess, K.-U., Dingwell, D.B., 2020. Rheological change and degassing during a trachytic Vulcanian eruption at Kilian volcano, Chaîne des Puys, France. Bull. Volcanol.

Costa, F., Andreastuti, S., Bouvet de Maisonneuve, C., Pallister, J.S., 2013. Petrological insights into the storage conditions, and magmatic processes that yielded the centennial 2010 Merapi explosive eruption. J. Volcanol. Geotherm. Res. 261, 209–235. https://doi.org/10.1016/j.jvolgeores.2012.12.025

Couch, S., Sparks, R.S.J., Carroll, M.R., 2003. The kinetics of degassing-induced crystallization at Soufrière Hills volcano, Montserrat. J. Petrol. 44, 1477–1502.

Degruyter, W., Burgisser, A., Bachmann, O., Malaspinas, O., 2010. Synchrotron X-ray microtomography and lattice Boltzmann simulations of gas flow through volcanic pumices. Geospheres 6, 470–481.

Devine, J.D., Rutherford, M.J., Norton, G.E., Young, S.R., 2003. Magma storage region processes inferred from geochemistry of Fe-Ti oxides in andesitic magma, Soufrière Hills volcano, Montserrat, W.I. J. Petrol. 44, 1375–1400.

Doube, M., 2020. Multithreaded two-pass connected components labelling and particle analysis in ImageJ. bioRxiv 2020.02.28.969139. https://doi.org/10.1101/2020.02.28.969139

Drignon, M.J., Bechon, T., Arbaret, L., Burgisser, A., Komorowski, J.-C., Caroline, M., Hayden, M., Yaputra, R., 2016. Preexplosive conduit conditions during the 2010 eruption of Merapi volcano (Java, Indonesia). Geophys. Res. Lett. 43, 11,595-11,602. https://doi.org/10.1002/2016GL071153

Druitt, T.H., Young, S.R., Baptie, B., Bonadonna, C., Calder, E.S., Clarke, A.B., Cole, P.D., Harford, C.L., Herd, R.A., Luckett, R., Ryan, G., Voight, B., 2002. Episodes of cyclic Vulcanian explosive activity with fountain collapse at Soufrière Hills Volcano, Montserrat. Geol. Soc. Lond. Mem. 21, 281–306. https://doi.org/10.1144/GSL.MEM.2002.021.01.13

Edmonds, M., Brett, A., Herd, R.A., Humphreys, M.C.S., Woods, A., 2015. Magnetite-bubble aggregates at mixing interfaces in andesite magma bodies. Geol. Soc. Lond. Spec. Publ. 410, 95–121. https://doi.org/10.1144/SP410.7

Erdmann, S., Martel, C., Pichavant, M., Bourdier, J.-L., Champallier, R., Komorowski, J.-C., Cholik, N., 2016. Constraints from Phase Equilibrium Experiments on Pre-eruptive Storage Conditions in Mixed Magma Systems: a Case Study on Crystal-rich Basaltic Andesites from Mount Merapi, Indonesia. J. Petrol. 57, 535–560. https://doi.org/10.1093/petrology/egw019

Fiege, A., Cichy, S.B., 2015. Experimental constraints on bubble formation and growth during magma ascent: A review. Am. Mineral. 100, 2426–2442. https://doi.org/10.2138/am-2015-5296

Gardner, J.E., 2007. Heterogeneous bubble nucleation in highly viscous silicate melts during instantaneous decompression from high pressure. Chem. Geol. 236, 1–12.

Gardner, J.E., Denis, M.-H., 2004. Heterogeneous bubble nucleation on Fe-Ti oxide crystals in high-silica rhyolitic melts. Geochim. Cosmochim. Acta 68, 3587–3597.

Ghiorso, M.S., Evans, B.W., 2008. Thermodynamics of Rhombohedral Oxide Solid Solutions and a Revision of the FE-TI Two-Oxide Geothermometer and Oxygen-Barometer. Am. J. Sci. 308, 957–1039. https://doi.org/10.2475/09.2008.01

Giachetti, T., Burgisser, A., Arbaret, L., Druitt, T.H., Kelfoun, K., 2011. Quantitative textural analysis of Vulcanian pyroclasts (Montserrat) using multi-scale X-ray computed microtomography: comparison with results from 2D image analysis. Bull. Volcanol. 73, 1295–1309. https://doi.org/10.1007/s00445-011-0472-1

Giachetti, T., Druitt, T.H., Burgisser, A., Arbaret, L., Galven, C., 2010. Bubble nucleation, growth and coalescence during the 1997 Vulcanian explosions of Soufrière Hills Volcano, Montserrat. J. Volcanol. Geotherm. Res. 193, 215–231.

Gualda, G.A.R., Anderson, A.T., 2007. Magnetite scavenging and the buoyancy of bubbles in magmas. Part 1: Discovery of a pre-eruptive bubble in Bishop rhyolite. Contrib. Mineral. Petrol. 153, 733–742. https://doi.org/10.1007/s00410-006-0173-5

Gualda, G.A.R., Ghiorso, M.S., Lemons, R.V., Carley, T.L., 2012. Rhyolite-MELTS: a Modified Calibration of MELTS Optimized for Silica-rich, Fluid-bearing Magmatic Systems. J. Petrol. 53, 875–890. https://doi.org/10.1093/petrology/egr080

Hammer, J., 2008. Experimental Studies of the Kinetics and energetics of Magma Crystallization. Rev. Mineral. Geochem. 69, 9–59.

Hurwitz, S., Navon, O., 1994. Bubble nucleation in rhyolitic melts: Experiments at high pressure, temperature, and water content. Earth Planet. Sci. Lett. 122, 267–280.

Jaquet, O., Sparks, R.S.J., Carniel, R., 2006. Magma memory recorded by statistics of volcanic explosions at the Soufrière Hills volcano, Montserrat. pp. 175-184 TY2-KW-0.

Knipping, J.L., Bilenker, L.D., Simon, A.C., Reich, M., Barra, F., Deditius, A.P., Lundstrom, C., Bindeman, I., Munizaga, R., 2015. Giant Kiruna-type deposits form by efficient flotation of magmatic magnetite suspensions. Geology 43, 591–594. https://doi.org/10.1130/G36650.1

Komorowski, J.-C., Jenkins, S., Baxter, P.J., Picquout, A., Lavigne, F., Charbonnier, S., Gertisser, R., Preece, K., Cholik, N.,. Budi-Santoso, A., Surono, -, 2013. Paroxysmal dome explosion during the Merapi 2010 eruption: Processes and facies relationships of associated high-energy pyroclastic density currents. J. Volcanol. Geotherm. Res. 261, 260–294.

Laumonier, M., Arbaret, L., Burgisser, A., Champallier, R., 2011. Porosity redistribution enhanced by strain localization in crystal-rich magmas. Geology 39, 715–718. https://doi.org/10.1130/G31803.1

Lensky, N.G., Navon, O., Lyakhovsky, V., 2004. Bubble growth during decompression of magma: experimental and theoretical investigation. J. Volcanol. Geotherm. Res. 129, 7–22.

Liu, Y., Zhang, Y., Behrens, H., 2005. Solubility of H2O in rhyolitic melts at low pressures and a new empirical model for mixed H2O-CO2 solubility in rhyolitic melts. J. Volcanol. Geotherm. Res. 143, 219–235.

Loughlin, S.C., Calder, E.S., Clarke, A., Cole, P.D., Luckett, R., Mangan, M.T., Pyle, D.M., Sparks, R.S.J., Voight, B., Watts, R.B., 2002. Pyroclastic flows and surges generated by the 25 June 1997 dome collapse, Soufrière Hills Volcano, Montserrat. Geol. Soc. Lond. Mem. 21, 191–209. https://doi.org/10.1144/GSL.MEM.2002.021.01.09

Loughlin, S.C., Luckett, R., Ryan, G., Christopher, T., Hards, V., De Angelis, S., Jones, L., Strutt, M., 2010. An overview of lava dome evolution, dome collapse and cyclicity at Soufrière Hills Volcano, Montserrat, 2005-2007. Geophys. Res. Lett. 37.

Mann, C.P., Wallace, P.J., Stix, J., 2013. Phenocryst-hosted melt inclusions record stalling of magma during ascent in the conduit and upper magma reservoir prior to vulcanian explosions, Soufrière Hills volcano, Montserrat, West Indies. Bull. Volcanol. 75, 687. https://doi.org/10.1007/s00445-013-0687-4

Martel, C., 2012. Eruption Dynamics Inferred from Microlite Crystallization Experiments: Application to Plinian and Dome-forming Eruptions of Mt. Pelée (Martinique, Lesser Antilles). J. Petrol. 53, 699–725.

Martel, C., Bourdier, J.-L., Pichavant, M., Traineau, H., 2000. Textures, water content and degassing of silicic andesites from recent Plinian and dome-forming eruptions at Mount Pelée volcano (Martinique, Lesser Antilles arc). J. Volcanol. Geotherm. Res. 96, 191–206.

Martel, C., Champallier, R., Prouteau, G., Pichavant, M., Arbaret, L., Balcone-Boissard, H., Boudon, G., Boivin, P., Bourdier, J.-L., Scaillet, B., 2013. Trachyte Phase Relations and Implication for Magma Storage Conditions in the Chaîne des Puys (French Massif Central). J. Petrol. 54, 1071–1107. https://doi.org/10.1093/petrology/egt006

Martel, C., Schmidt, B.C., 2003. Decompression experiments as an insight into ascent rates of silicic magmas. Contrib. Mineral. Petrol. 144, 397–415.

Mason, R.M., Starostin, A.B., Melnik, O.E., Sparks, R.S.J., 2006. From Vulcanian explosions to sustained explosive eruptions: The role of diffusive mass transfer in conduit flow dynamics. J. Volcanol. Geotherm. Res. 153, 148–165.

Mattews, S.J., Gardeweg, M.C., Sparks, R.S.J., 1997. The 1984 to 1996 cyclic activity of Lascar Volcano, northern Chile: cycles of dome growth, dome subsidence, degassing and explosive eruptions. Bull. Volcanol. 59, 72–82.

Melnik, O.E., Blundy, J.D., Rust, A.C., Muir, D.D., 2011. Subvolcanic plumbing systems imaged through crystal size distributions. Geology 39, 403–406.

Miwa, T., Geshi, N., 2012. Decompression rate of magma at fragmentation: Inference from broken crystals in pumice of vulcanian eruption. J. Volcanol. Geotherm. Res. 227–228, 76–84.

Moitra, P., Gonnermann, H.M., Houghton, B.F., Giachetti, T., 2013. Relating vesicle shapes in pyroclasts to eruption styles. Bull. Volcanol. 75, 691.

Muir, D.D., Blundy, J.D., Rust, A.C., 2012. Multiphase petrography of volcanic rocks using element maps: a method applied to Mount St. Helens, 1980–2005. Bull. Volcanol. 74, 1101–1120. https://doi.org/10.1007/s00445-012-0586-0

Mujin, M., Nakamura, M., 2014. A nanolite record of eruption style transition. Geology 42, 611–614. https://doi.org/10.1130/G35553.1

Murch, A.P., Cole, P.D., 2019. Using microlites to gain insights into ascent conditions of differing styles of volcanism at Soufrière Hills Volcano. J. Volcanol. Geotherm. Res. 384, 221–231. https://doi.org/10.1016/j.jvolgeores.2019.07.022

Nadeau, O., Williams-Jones, A.E., Stix, J., 2013. Magmatic-hydrothermal evolution and devolatilization beneath Merapi volcano, Indonesia. J. Volcanol. Geotherm. Res. 261, 50–68.

Pistolesi, M., Cioni, R., Bonadonna, C., Elissondo, M., Baumann, V., Bertagnini, A., Chiari, L., Gonzales, R., Rosi, M., Francalanci, L., 2015. Complex dynamics of small-moderate volcanic events: the example of the 2011 rhyolitic Cordón Caulle eruption, Chile. Bull. Volcanol. 77, 3. https://doi.org/10.1007/s00445-014-0898-3

Pleše, P., Higgins, M.D., Baker, D.R., Kudrna Prašek, M., 2019a. Nucleation and growth of bubbles on plagioclase crystals during experimental decompression degassing of andesitic melts. J. Volcanol. Geotherm. Res. 388, 106679. https://doi.org/10.1016/j.jvolgeores.2019.106679

Pleše, P., Higgins, M.D., Baker, D.R., Lanzafame, G., Kudrna Prašek, M., Mancini, L., Rooyakkers, S.M., 2019b. Production and detachment of oxide crystal shells on bubble walls during experimental vesiculation of andesitic magmas. Contrib. Mineral. Petrol. 174, 21. https://doi.org/10.1007/s00410-019-1556-8

Pleše, P., Higgins, M.D., Mancini, L., Lanzafame, G., Brun, F., Fife, J.L., Casselman, J., Baker, D.R., 2018. Dynamic observations of vesiculation reveal the role of silicate crystals in bubble nucleation and growth in andesitic magmas. Lithos 296–299, 532–546. https://doi.org/10.1016/j.lithos.2017.11.024

Preece, K., Gertisser, R., Barclay, J., Berlo, K., Herd, R.A., Edinburgh Ion Microprobe Facility, -, 2014. Pre- and syn-eruptive degassing and crystallisation processes of the 2010 and 2006 eruptions of Merapi volcano, Indonesia. Contrib. Mineral. Petrol. 168, 1061.

Richard, D., Scheu, B., Mueller, S.P., Spieler, O., Dingwell, D.B., 2013. Outgassing: Influence on speed of magma fragmentation. J. Geophys. Res. Solid Earth 118, 862–877. https://doi.org/10.1002/jgrb.50080

Sano, K., Wada, K., Sato, E., 2015. Rates of water exsolution and magma ascent inferred from microstructures and chemical analyses of the Tokachi–Ishizawa obsidian lava, Shirataki, northern Hokkaido, Japan. J. Volcanol. Geotherm. Res. 292, 29–40. https://doi.org/10.1016/j.jvolgeores.2014.11.015

Schindelin, J., Arganda-Carreras, I., Frise, E., Kaynig, V., Longair, M., Pietzsch, T., Preibisch, S., Rueden, C., Saalfeld, S., Schmid, B., Tinevez, J.-Y., White, D.J., Hartenstein, V., Eliceiri, K.,

Tomancak, P., Cardona, A., 2012. Fiji: an open-source platform for biological-image analysis. Nat. Methods 9, 676–682. https://doi.org/10.1038/nmeth.2019

Shea, T., 2017. Bubble nucleation in magmas: A dominantly heterogeneous process? J. Volcanol. Geotherm. Res. 343, 155–170. https://doi.org/10.1016/j.jvolgeores.2017.06.025

Shea, T., Gurioli, L., Larsen, J.F., Houghton, B.F., Hammer, J.E., Cashman, K.V., 2010. Linking experimental and natural vesicle textures in Vesuvius 79 AD white pumice. J. Volcanol. Geotherm. Res. 192, 69–84.

Sparks, R.S.J., Gardeweg, M.C., Calder, E.S., Matthews, S.J., 1997. Erosion by pyroclastic flows on Lascar Volcano, Chile. Bull. Volcanol. 58, 557–565. https://doi.org/10.1007/s004450050162

Stampanoni, M., Groso, A., Isenegger, A., Mikuljan, G., Chen, Q., Bertrand, A., Henein, S., Betemps, R., Frommherz, U., Böhler, P., Meister, D., Lange, M., Abela, R., 2006. Trends in synchrotron-based tomographic imaging: the SLS experience, in: Developments in X-Ray Tomography V. Presented at the Developments in X-Ray Tomography V, International Society for Optics and Photonics, p. 63180M. https://doi.org/10.1117/12.679497

Suzuki, Y., Fujii, T., 2010. Effect of syneruptive decompression path on shifting intensity in basaltic sub-Plinian eruption: Implication of microlites in Yufune-2 scoria from Fuji volcano, Japan. J. Volcanol. Geotherm. Res. 198, 158–176. https://doi.org/10.1016/j.jvolgeores.2010.08.020

Taisne, B., Jaupart, C., 2008. Magma degassing and intermittent lava dome growth. Geophys. Res. Lett. 35.

Toramaru, A., 2006. BND (bubble number density) decompression rate meter for explosive volcanic eruptions. J. Volcanol. Geotherm. Res. 154, 303–316.

Toramaru, A., 1995. Numerical study of nucleation and growth of bubbles in viscous magmas. J. Geophys. Res. 100, 1913–1931.

Toramaru, A., Noguchi, S., Oyoshihara, S., Tsune, A., 2008. MND(microlite number density) water exsolution rate meter. J. Volcanol. Geotherm. Res., Scientific drilling at Mount Unzen 175, 156–167. https://doi.org/10.1016/j.jvolgeores.2008.03.035

Venezky, D.Y., Rutherford, M.J., 1999. Petrology and Fe-Ti oxide reequilibration of the 1991 Mount Unzen mixed magma. J. Volcanol. Geotherm. Res. 89, 213–230.

Widiyantoro, S., Ramdhan, M., Métaxian, J.-P., Cummins, P.R., Martel, C., Erdmann, S., Nugraha, A.D., Budi-Santoso, A., Laurin, A., Fahmi, A.A., 2018. Seismic imaging and petrology explain highly explosive eruptions of Merapi Volcano, Indonesia. Sci. Rep. 8. https://doi.org/10.1038/s41598-018-31293-w

Wright, H.M.N., Weinberg, R.F., 2009. Strain localization in vesicular magma: Implications for rheology and fragmentation. Geology 37, 1023–1026.

Figure Captions

Figure 1: Three‑dimensional cumulative (open circles) and non‑cumulative (gray bars) oxide size distributions in experimental sample ABG28. The two vertical black lines indicate the lower limits of detection of the other experimental samples.

Figure 2: Oxide connectivity (fraction of oxides connected to vesicles) as a function of VOI size. The counting method in each VOI used object centroids (see Fig. S3 for details). VOIs of natural samples $>10^8$ voxels are statistically representative of connectivity. VOIs of experimental samples $>10^7$ voxels are statistically representative of connectivity. Dimensions of the largest VOIs are given in Table S2.

Figure 3: Vesicle number density (VND) as a function of oxide number density (OND) of two characteristic samples that were studied using different methods. Intrinsic errors are smaller than the symbols.

Figure 4: Representative SEM and thresholded images of natural products. Our procedure distinguishes four types of objects (vesicles, oxides, other crystals, and glass). SEM images occupy the upper left parts and thresholded images occupy the lower right parts. Horizontal white scale bars are 100 μm long. A) Vesicular texture (AMO36B). B) Diktytaxitic texture (AMO16C1). C) Intermediate texture (1448).

Figure 5: Levels of oxide–vesicle (x-axis) and vesicle–oxide (y-axis) connectivity reported as proportion of objects in contact. Insets illustrate four pairs of connectivity levels (black squares are oxides and gray disks are vesicles). Open triangles represent natural samples sorted by texture: diktytaxitic ("dik.") and pumiceous ("other"). Black triangles represent experimental samples. Errors smaller than symbols are not shown.

Figure 6: Representative 3D and slice renderings from μCT scans of experimental and natural products. A) Grayscale slice of natural sample AMO29. Vesicles are dark gray; glass and plagioclase share a similar medium gray shade; pyroxene and amphibole share a similar shade of light gray, and oxides are white. Scale bar is 1 mm. B) Natural sample AMO29. Oxides are red, glass and other minerals are blue, and vesicles are transparent. Scale bar is 100 μm. C) Experimental sample ABG16. Vesicles are blue, oxides are red, and glass is transparent. Scale bar is 50 μm.

Figure 7: Vesicle number density (VND) as a function of oxide number density (OND) of natural and experimental samples. Vertical lines represent diktytaxitic samples for which only ONDs are reported. A) Experimental data. Errors associated to the Burgisser and Gardner (2004) samples are smaller than the symbols. B) Eruptions dominated by vertical explosions. SHV stands for Soufrère Hills volcano samples and BAF stands for block-and-ash flow samples. Vertical errors bars of the Kilian samples extend from the VND of the full vesicle population (open squares) down to that including only the smallest vesicles (Colombier et al., 2017). Black error bars indicate typical errors (see the Methods section). C) Eruptions dominated by dome collapse. Black error bars indicate typical errors.

Figure 8: OND as a function of the pressure difference between the reservoir and the conduit. Pre-explosive conduit storage pressures for Soufrière Hills (SHV, triangles) are from Burgisser et al. (2010) for the 1997 explosions, from Burgisser et al. (2019) for the 2010 explosion, and from Table S1 for the 2006 block-and-ash flow. Pressures for Kilian (squares) are from Colombier et al. (2017) and pressures for Merapi (circles) are from Drignon et al. (2016). Errors on pressures were omitted for clarity.

Figure 9: Syn-explosive decompression rates from VND as a function of pre-explosive storage

41

pressure for Soufrière Hills (SHV), Kilian (Colombier et al., 2017), and Merapi volcanoes. Errors were omitted for clarity.

Figure 10: OND (top axis) and crystallization rate (bottom axis) as a function of pre-explosive storage pressures. A) Data from two series of Vulcanian events (1997 and 2010) at Soufrière Hills volcano. Crystallization curves are given for magnetite and ilmenite. B) Data from two events (Vulcanian on Oct. 26 and sub-Plinian on Nov. 5) at Merapi volcano. Magnetite is the only precipitating oxide. Crystallization curves are given for each of the three magmas involved in the eruption (deep, shallow, and recharge).

Figure 11: Frequency distribution of ascent rates stemming from the Toramaru et al. (2008) decompression meter (Text S5). Ascent rates are calculated from individual OND determinations at the melt water contents and microlite nucleation pressures indicated. A) Soufrière Hills volcano. B) Merapi volcano.

Figure 12: Ascent dynamics at Kilian volcano. A) OND (top axis) and magnetite crystallization rate (bottom axis) as a function of pre-explosive storage pressures. Initial conditions of the rhyolite-MELTS runs are given in Supplementary Text S4. B) Frequency distribution of ascent rates stemming from the Toramaru et al. (2008) decompression meter (Text S5).

Credits author statement
AB, LA, CM: Conceptualization, Investigation; MF, MC: Investigation; All : Writing - Review & Editing

Declaration of interests

☒ The authors declare that they have no known competing financial interests or personal relationships that could have appeared to influence the work reported in this paper.

☐The authors declare the following financial interests/personal relationships which may be considered as potential competing interests:

Highlights

- Measures of oxide microlites number densities in products of silicic eruptions are scarce.
- We measured oxide and vesicle number densities in experiments and at five volcanoes.
- Heterogeneous nucleation models only work when oxides are at least as numerous as vesicles.
- Ascent rates needed to nucleate oxides overlap those characteristic of the effusive–explosive transition.
- The appearance of oxides in the conduit is a primer for explosive behavior.
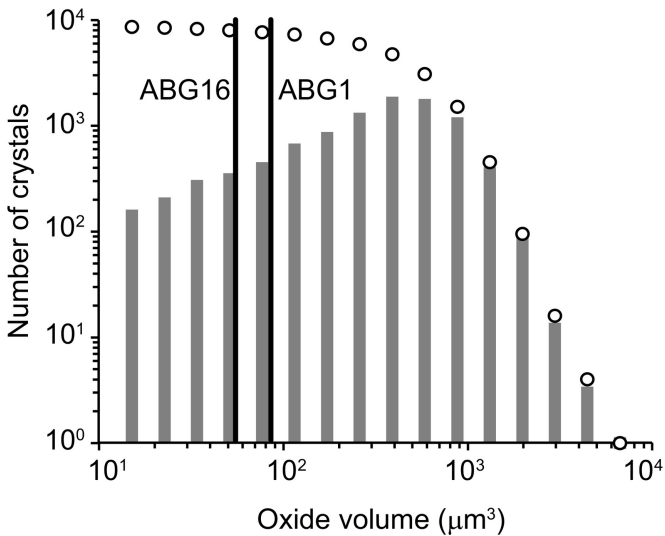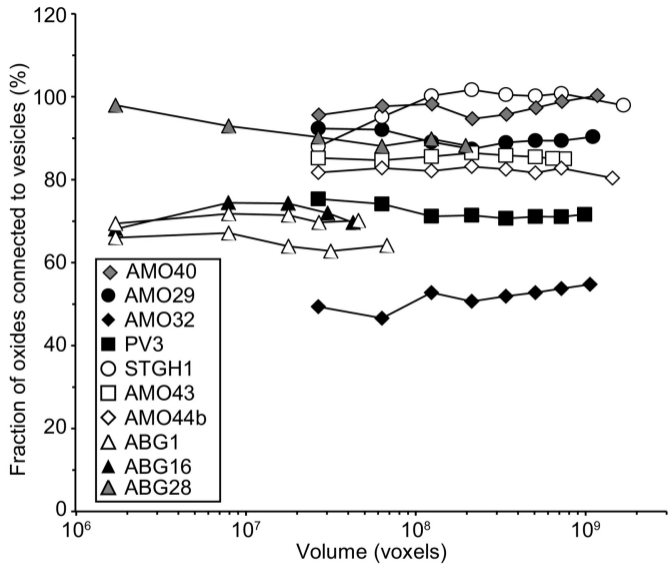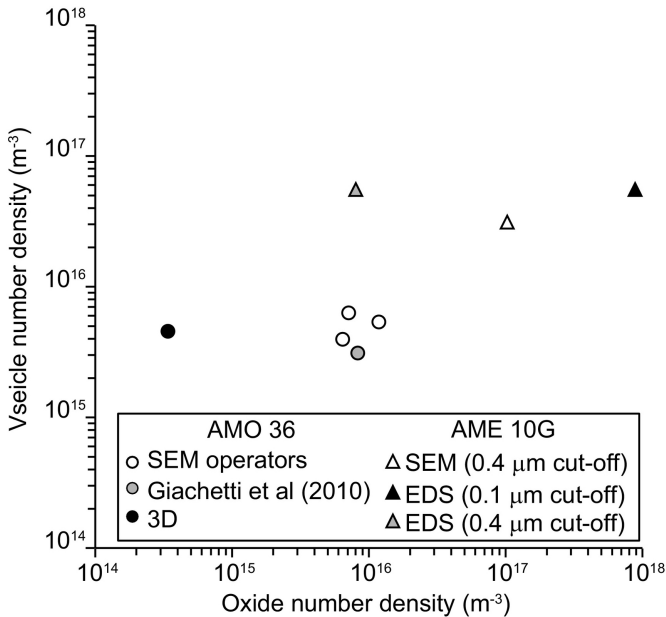
Figure 1

Figure 2

Figure 3
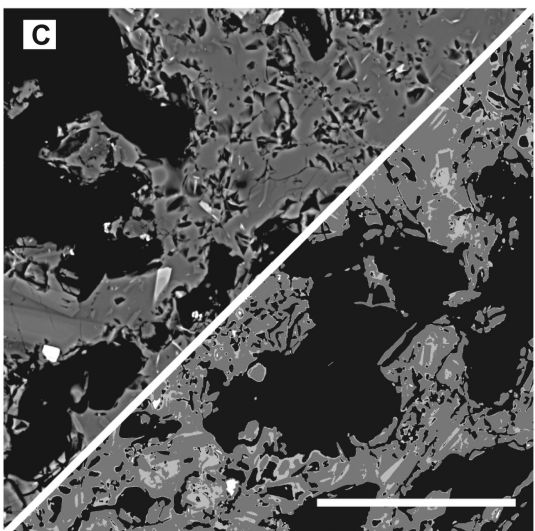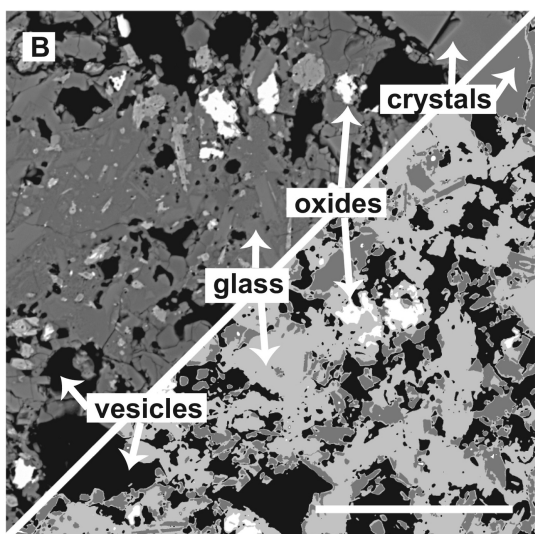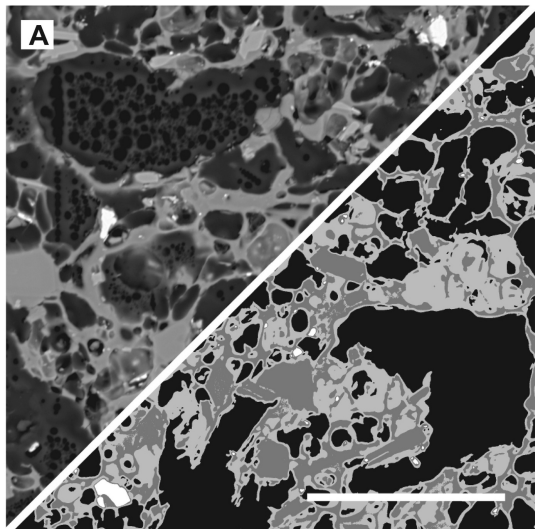
Figure 4
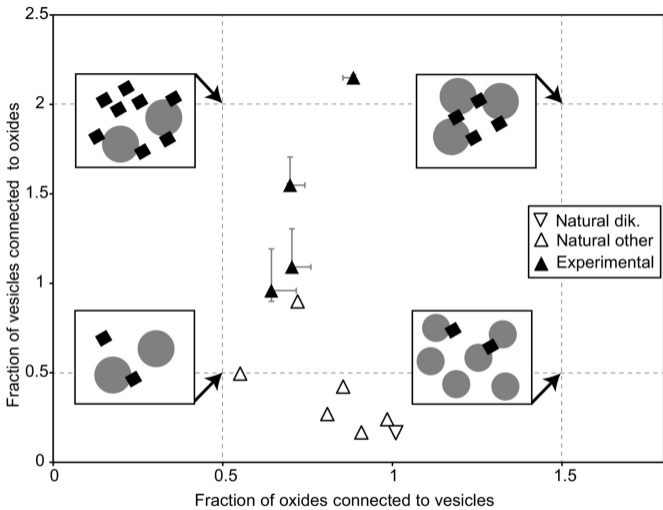
Figure 5
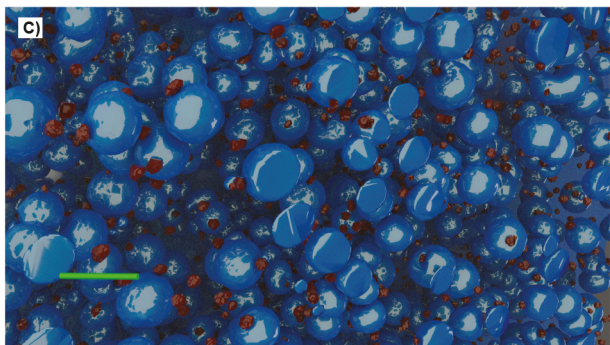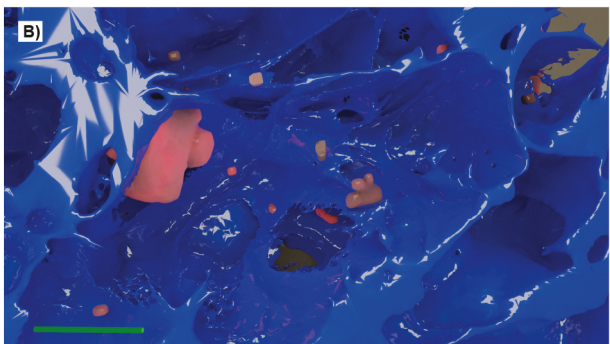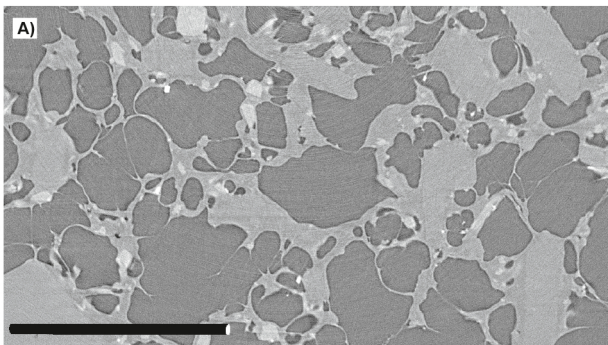
Figure 6
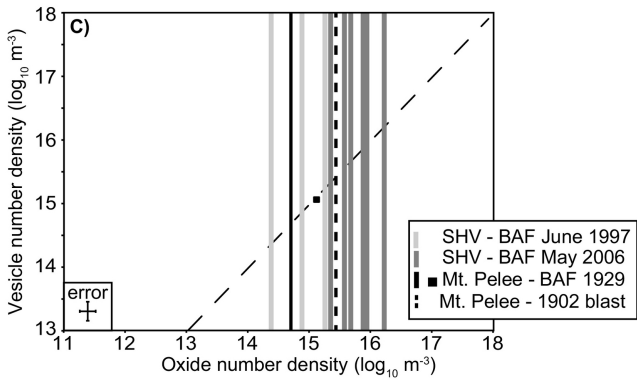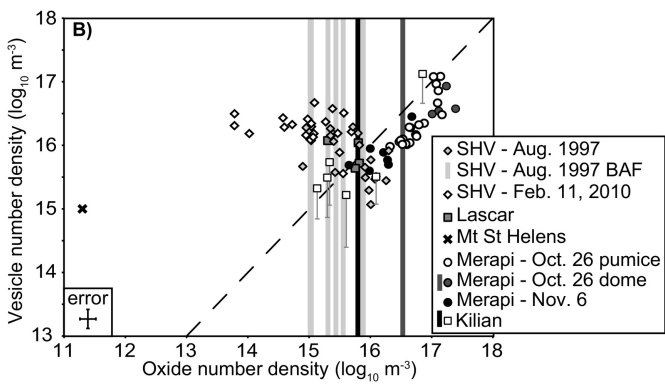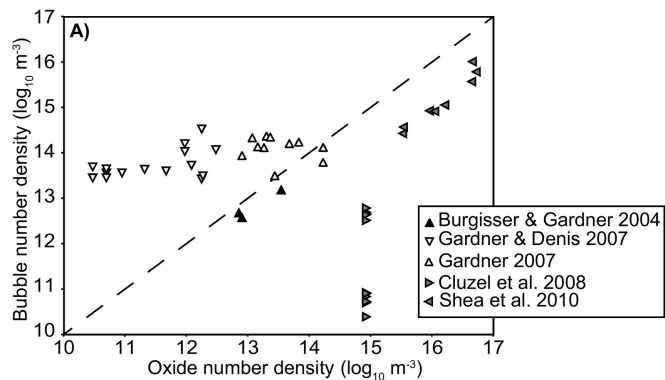
Figure 7
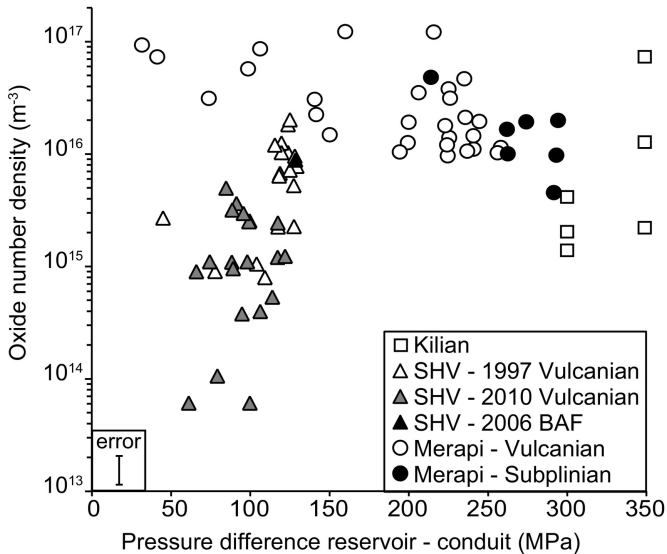
Figure 8
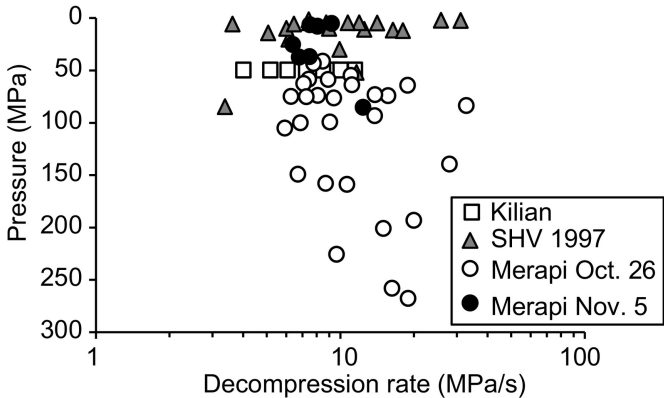
Figure 9
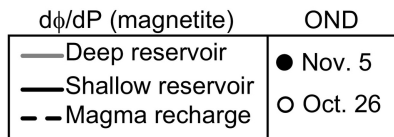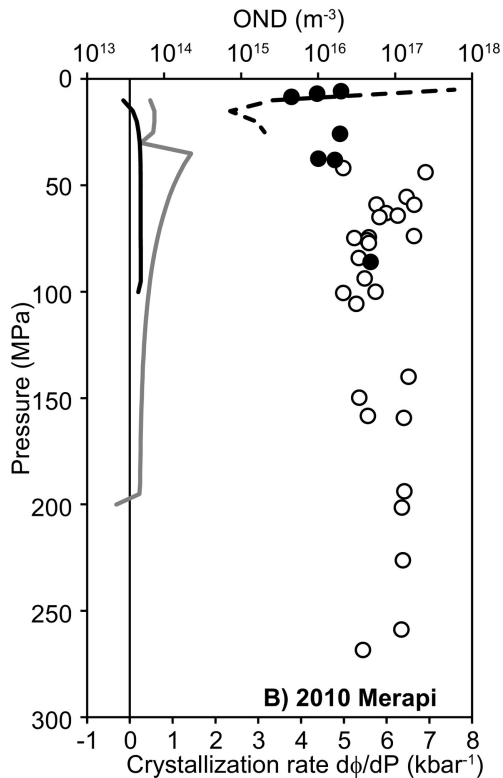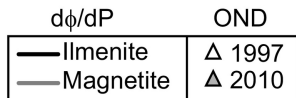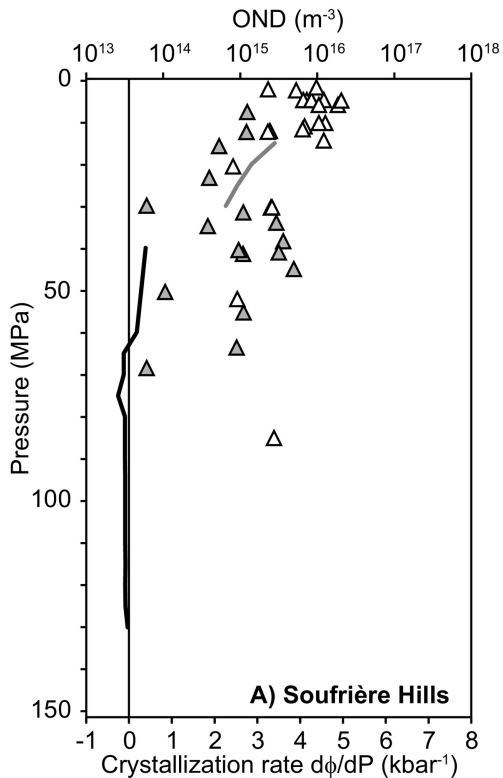
Figure 10

A) Soufrière Hills
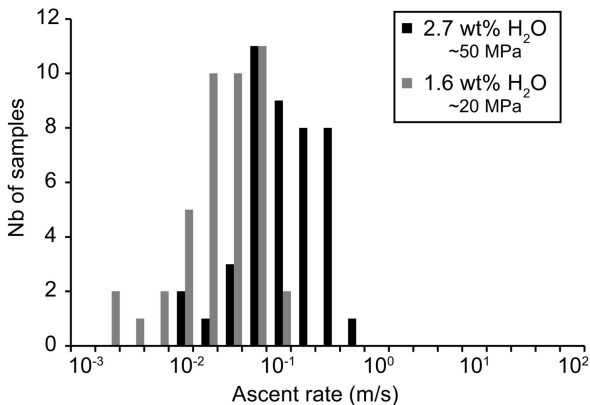
B) Merapi

Figure 11

Figure 12